

Original Manuscript

Toxicogenomics analysis of mouse lung responses following exposure to titanium dioxide nanomaterials reveal their disease potential at high doses

Luna Rahman¹, Dongmei Wu¹, Michael Johnston², Andrew William¹ and Sabina Halappanavar^{1,*}

¹Environmental Health Science and Research Bureau, Health Canada, Tunney's Pasture Bldg. 8, Ottawa, Ontario K1A 0K9, Canada and ²Centre for Biologics Evaluation, Biologics and Genetic Therapies Directorate, Health Canada, Ottawa, Ontario K1A 0K9, Canada

*To whom correspondence should be addressed: Tel: 613 957 3136; Fax: 613 941 8530; Email: sabina.halappanavar@hc-sc.gc.ca

Received 24 June 2016; Revised 4 August 2016; Accepted 30 August 2016.

Abstract

Titanium dioxide nanoparticles (TiO₂NPs) induce lung inflammation in experimental animals. In this study, we conducted a comprehensive toxicogenomic analysis of lung responses in mice exposed to six individual TiO₂NPs exhibiting different sizes (8, 20 and 300 nm), crystalline structure (anatase, rutile or anatase/rutile) and surface modifications (hydrophobic or hydrophilic) to investigate whether the mechanisms leading to TiO₂NP-induced lung inflammation are property specific. A detailed histopathological analysis was conducted to investigate the long-term disease implications of acute exposure to TiO₂NPs. C57BL/6 mice were exposed to 18, 54, 162 or 486 µg of TiO₂NPs/mouse via single intratracheal instillation. Controls were exposed to dispersion medium only. Bronchoalveolar lavage fluid (BALF) and lung tissue were sampled on 1, 28 and 90 days post-exposure. Although all TiO₂NPs induced lung inflammation as measured by the neutrophil influx in BALF, rutile-type TiO₂NPs induced higher inflammation with the hydrophilic rutile TiO₂NP showing the maximum increase. Accordingly, the rutile TiO₂NPs induced higher number of differentially expressed genes. Histopathological analysis of lung sections on Day 90 post-exposure showed increased collagen staining and fibrosis-like changes following exposure to the rutile TiO₂NPs at the highest dose tested. Among the anatase, the smallest TiO₂NP of 8 nm showed the maximum response. The anatase TiO₂NP of 300 nm was the least responsive of all. The results suggest that the severity of lung inflammation is property specific; however, the underlying mechanisms (genes and pathways perturbed) leading to inflammation were the same for all particle types. While the particle size clearly influenced the overall acute lung responses, a combination of small size, crystalline structure and hydrophilic surface contributed to the long-term pathological effects observed at the highest dose (486 µg/mouse). Although the dose at which the pathological changes were observed is considered physiologically high, the study highlights the disease potential of certain TiO₂NPs of specific properties.

Introduction

Globally, titanium dioxide nanoparticles (TiO₂NPs) are among the most widely produced and used nanomaterials (NMs). The estimated

global annual production of TiO₂NPs is currently near 12,500 tons (1,2). This value is expected to reach 2.5 million metric tons by 2025 (3). Owing to their unique physico-chemical properties, TiO₂NPs are used in diverse applications including consumer, industrial

and biomedical fields. The extensive synthesis and pervasive use of TiO₂NPs has resulted in unprecedented avenues for human exposure to these materials in the environment and through the use of consumer products. Exposure to TiO₂NPs via inhalation leads to pulmonary inflammation, emphysema and lung injury in experimental rodents (4,5). Due to their nanosize, TiO₂NPs penetrate deep into the highly vascularised areas of lungs and persist in lungs for weeks after the last exposure (6). In addition, TiO₂NPs deposited in rodent lungs translocate to blood, liver, heart, lymph nodes, spleen and other organs (7–10). These results imply that exposure to TiO₂NPs can negatively impact health of the organisms exposed.

Acute pulmonary responses in rodents exposed to TiO₂NPs are greatly influenced by their primary particle size (11–14), surface area, surface charge, surface coatings (15–18) and their crystalline structure (19,20). These results suggest that a combination of physico-chemical properties influence the pulmonary outcome of exposure to TiO₂NPs. It is yet to be determined whether one of these properties is more important than the others and whether the underlying mechanisms of the observed pulmonary responses differ by the properties of TiO₂NPs.

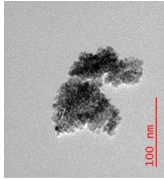
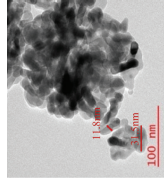
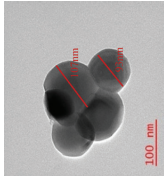
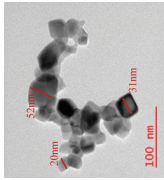
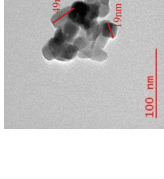
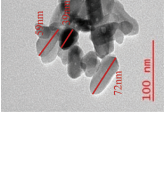
We have previously employed toxicogenomics tools to characterise the pulmonary transcriptomic responses in mice exposed via inhalation (21) or instillation to TiO₂NPs of different sizes, surface coatings and TiO₂NPs embedded in paint (6). We have shown that all types of TiO₂NPs induce pulmonary inflammation via the same mechanisms; however, the severity of response varies with their specific properties (22). The transcriptomic studies discussed above were limited to few TiO₂NP types and for now, it is not clear whether the results from those studies can be generalised to all TiO₂NP variants. In the present study, we conducted a comprehensive investigation of lung toxicogenic responses in mice exposed individually to six different types of TiO₂NPs varying in size, crystalline structure and surface coatings to further our understanding of the underlying mechanisms of TiO₂NP-induced lung responses. Acute, subchronic and chronic post-exposure time points were included along with a range of doses. The TiO₂NP types included anatase TiO₂NPs of 8, 20, and 300 nm, mixed anatase/rutile TiO₂NP of 20 nm and rutile TiO₂NPs of 20 nm with hydrophilic or hydrophobic surfaces. Mice were exposed via single intratracheal instillation to 18, 54, 162 or 486 µg/animal doses of individual TiO₂NPs. Although the 486 µg/animal dose is physiologically high, it was included in the study to determine whether exposure to TiO₂NPs results in lung pathology at higher doses. Samples were collected at 1, 28 and 90 days post-exposure. Bronchoalveolar lavage fluid (BALF) cellularity, histopathology, particle localization in lungs (by transmission electron microscopy (TEM) and Cytoviva nanoscale hyperspectral microscopy) were assessed at all three post-exposure time points. Global gene expression profiles were generated for all doses, at Day 1 and Day 28 post-exposure time points. Pathway tools were employed to characterise the molecular pathways perturbed following exposure to TiO₂NPs. Disease similarity tools were employed to determine whether the altered gene expression profiles are associated with any known lung disease.

Methods

TiO₂NPs investigated

A set of six TiO₂NPs of varying physico-chemical properties were investigated in the current study (Table 1): anatase TiO₂NPs of three different sizes, 8, 20 and 300 nm (^aTiO₂⁸, ^aTiO₂²⁰ and ^aTiO₂³⁰⁰), mixed anatase and rutile TiO₂NPs of 20 nm (^{ra}TiO₂²⁰) and rutile

Table 1. Physico-chemical properties of TiO₂NPs.

NMs	^a TiO ₂ ⁸	^a TiO ₂ ²⁰	^a TiO ₂ ³⁰⁰	^{ra} TiO ₂ ²⁰	^r TiO ₂ ²⁰ (HY)	^r TiO ₂ ²⁰ (HP)
TEM ^b						
Crystal structure ^b	Anatase	Anatase	Anatase	Rutile/anatase (81.5:18.5)	Rutile	Rutile
Primary size ^b (nm)	8 (XRD)	20 (XRD)	300 (XRD)	22/40 (XRD)	20 (XRD)	21 (XRD)
Surface area ^b (m ² /g)	234.47–229.00	90	10	52.81–55.49	51.69–50.86	57.07–57.18
Particle size DLS ^c (nm)	148	242.9	130.1	242.9	110.1	39.3
Surface modification ^b	modified	none	none	none	Modified Dimethicone	Modified Glycerol
Impurities ^b	Al, Si, Na, P, S, Zr	none	Al, Zr, polyalcohol	none	Al, Si, Fe and S	Al, Si, S
Hydrophilicity/hydrophobicity ^b	Hydrophilic	none	Hydrophilic	Hydrophilic	Hydrophobic	Hydrophilic

^aNano Imaging Facility of Carleton University, Ottawa, Ontario, Canada.

^bAvailable at: <http://publications.jrc.ec.europa.eu/repository/handle/JRC86291>.

^cCenter for Biologics Evaluation (CBE), Health Canada, Ottawa, Ontario, Canada.

TiO₂NPs of 20 nm with hydrophilic [^rTiO₂²⁰ (HY)] or hydrophobic [^rTiO₂²⁰ (HP)] surfaces. All six particles were obtained from the Organisation for Economic Co-operation and Development through the sponsorship program. The ^aTiO₂⁸ is commercially known as Hombikat UV100 and is available through Sachtleben Chemie GmbH, Germany. It is used as a semiconductor catalyst in photocatalytic applications. The ^aTiO₂²⁰ and ^aTiO₂³⁰⁰ are commercially available as PC105 and tiona, respectively, from Cristal Global (<http://www.cristal.com>), whereas, ^{ra}TiO₂²⁰ is commercially known as P25 and is available from Evonik Degussa GmbH, Germany. The ^rTiO₂²⁰ (HY) and ^rTiO₂²⁰ (HP) are known as UV Titan M262 and UV Titan M212, respectively, and are available from Sachtleben Chemie GmbH, Germany. The selected anatase TiO₂NPs are used in building materials and in air purification systems for their photocatalytic activity. They are also used in self-cleaning fabrics, glass and other products. The ^{ra}TiO₂²⁰ NPs are commonly used as catalyst carriers, active components for photocatalytic reactions and as heat stabilizers in silicone rubber. The two functionalised TiO₂NPs—^rTiO₂²⁰ (HY) and ^rTiO₂²⁰ (HP)—are used in skin and sun care products. The hydrophobic ^rTiO₂²⁰ (HY) is also used in manufacturing waterproof and stain resistant textiles (23,24).

Physico-chemical properties of TiO₂NPs

The particles ^aTiO₂⁸, ^{ra}TiO₂²⁰, ^rTiO₂²⁰ (HY) and ^rTiO₂²⁰ (HP) have been extensively characterised by the European Commission's Joint Research Centre (JRC) and reported in Rasmussen et al. (25). In brief, ^aTiO₂⁸ and ^{ra}TiO₂²⁰ are relatively pure. Negligible amount of silica (Si), aluminium (Al), and sulphur (S) was identified in ^aTiO₂⁸. The ^rTiO₂²⁰ (HY) and ^rTiO₂²⁰ (HP) contain 91.3% and 92.7% Ti, respectively, and are suggested to contain relatively higher levels of Al, Si, and S. In addition, gas chromatography–mass spectrometry analysis shows the presence of dimethicone (~2 weight %) coating on ^rTiO₂²⁰(HY) and glycerol (~1–2 weight %) on ^rTiO₂²⁰(HP), which contribute to the hydrophobic and hydrophilic nature of the ^rTiO₂²⁰ (HY) and ^rTiO₂²⁰ (HP), respectively (25). Extensive characterisations of ^aTiO₂²⁰ and ^aTiO₂³⁰⁰ have not been reported. The details of the particle characterisations are summarized in Table 1.

Preparation of TiO₂NP stocks for the exposure

A pilot study was conducted to assess the dispersion of TiO₂NPs in MilliQ water, 2% serum or mouse BALF. The results revealed (data not shown) that with the exception of ^{ra}TiO₂²⁰, all other TiO₂NPs are best dispersed in MilliQ water. Thus, MilliQ water was used as particle dispersion vehicle for the experiments. For the purposes of consistency, the ^{ra}TiO₂²⁰ was also prepared in MilliQ water. A stock suspension of 6 mL for each type of TiO₂NPs at a concentration of 12.15 mg/mL was made in MilliQ water. The particle suspension was dispersed by sonicating the samples using an S-450D sonifier (Branson Ultrasonics Corp., Danbury, CT, USA) at 10% amplitude for a total of 16 min on ice with alternating 10 s pulses and pauses in an enclosed chamber.

TEM analysis

The size and agglomeration state of TiO₂NPs in dry state were analysed using TEM analysis (Tecnai G2 F20 FETEM, FEI, Hillsboro, Oregon, USA) at the Nano Imaging Facility of Carleton University. Samples were stirred in filtered ethanol and sonicated for 5 min (ultrasonic water bath). A drop of this suspension was deposited on copper TEM grids (200-mesh copper grids covered with Formvar/Carbon film (Agar Scientific, Essex, UK), air-dried and analysed using TEM.

Dynamic light scattering analysis

The stock suspensions of the TiO₂NPs at a concentration of 50 µg/mL were prepared in MilliQ water and sonicated as described above. Prior to the dynamic light scattering (DLS) analysis with the Nicomp 380 ZLS instrument (Nicom Particle Sizing Systems, Santa Barbara, CA, USA), samples were manually mixed and diluted 1 in 100 with 0.22 µm-filtered MilliQ water and were sonicated again for 5 min in a water bath sonicator. The DLS instrument was calibrated using 90 nm and 240 nm standard calibration beads, and the analysis was conducted according to the DLS manufacturers' instructions. The value of the number-weighted particle size distribution was calculated assuming that the particles are spheres of uniform density that scatter light according to classical Mie theory (26).

Animal handling

Five-to-seven-week-old female C57BL/6 mice (Jackson Laboratory, Bar Harbor, ME, USA) were housed in autoclaved cages with a 12-h light–dark cycle. All mice were given food and water *ad libitum* throughout the experiment. Animals were weighed before beginning the exposure and once every week during the course of the experiment. Mice were housed in pairs. All animal procedures were conducted in accordance with the guidelines of the Canadian Council for Animal Care and approved by Health Canada's Animal Care Committee.

The particle suspensions were dispersed as described above under preparation of TiO₂NP stocks section. The 486 µg/40 µL stock suspensions of the TiO₂NPs were diluted to obtain 18, 54, and 162 µg per 40 µL and dispersed by sonication for an additional minute. The doses 18, 54, 162 and 486 µg/mouse are equivalent to 1.5, 5, 15, and 45 working days at the Danish occupational exposure level for TiO₂ (6.0 mg Ti/m³–9.75 mg TiO₂/m³), respectively. Although physiologically high, the dose 486 µg/mouse was included in the study to determine whether TiO₂NPs induce pathological changes at the higher doses. The suspensions were used immediately after the preparation. MilliQ water devoid of particles was used to expose control animals.

Exposure of mice and harvesting of biological samples

Each treatment group consisted of 10 animals. Mice in the experimental groups received a single intratracheal instillation of 18 µg (very low), 54 µg (low dose), 162 µg (medium dose) or 486 µg (high dose) of TiO₂NPs in a 40-µL suspension prepared as described above, followed by 150 µL air with a 250 µL SGE glass syringe (250F-LT-GT, MicroLab, Aarhus, Denmark). Intratracheal instillation was performed under anaesthesia with 5% isoflurane (Isoflo, Esteve Farma, Carnaxide, Portugal) in 100% oxygen. Control mice received 40 µL of vehicle (MilliQ water) only. Following instillation, mice were kept under observation until they recovered from anaesthesia. Mice were killed on Days 1, 28 and 90 post-exposure. Blood, BALF and lung tissue were collected. One set of five experimental and five control mice were lavaged and the left lobe of lung from these mice were cut into two pieces, snap frozen in liquid nitrogen and stored in cryogenic vials at –80°C until analysis. The other set of five experimental and five control mice were not lavaged. Whole lungs from these mice were fixed in formalin (three mice/group) or glutaraldehyde (two mice/group) for histopathology and TEM analysis, respectively. Various end points investigated at the different post-exposure time points are listed in Figure 1.

BALF analysis

One set of five mice from control and treated groups were lavaged as described in Poulsen et al. (27). In brief, a total of 2 mL of 0.9%

A summary of toxicity endpoints assessed at different post-exposure time points

Exposure: Five-to-seven week old female C57BL/6 mice were instilled once with 0, 18*, 54, 162 and 486 µg/animal of individual titanium dioxide nanomaterials.

Samples collected: BALF, Lung tissues

Toxicity end points studied		
Day1	Day28	Day90
<ul style="list-style-type: none"> •BALF cell counts •TEM analysis of lung sections •Histopathology analysis of lung sections – H&E stain •Global gene expression analysis •NAG activity in BALF •ALP activity in BALF 	<ul style="list-style-type: none"> •BALF cell counts •TEM analysis of lung sections •Histopathology analysis of lung sections – H&E, Trichrome stain •Global gene expression analysis 	<ul style="list-style-type: none"> •BALF cell counts •TEM analysis of lung sections •Histopathology analysis of lung sections – H&E, Trichrome stain •Global gene expression analysis •NAG activity in BALF •ALP activity in BALF

* 18µg dose was only assessed for BALF cell counts and cytotoxicity. Since the results showed no significant changes, this dose group was not included in the rest of the analysis.

Figure 1. Schematic representation of the toxicity end points assessed at various post-exposure time points.

sterile saline was injected in lungs and was recovered. The BALF was immediately put on ice until further processing. BALF was centrifuged at 4°C and 400 g for 10 min to collect cells, which were resuspended in 0.5 mL PBS.

Differential cell counts

The BALF cytopspins were prepared as described by Poulsen et al. (27) previously. The cytopspins were fixed with two sprays of Sheldon Cell Fix and air-dried and stained with haematoxylin and eosin (H & E). A total of 500 cells were counted per cytopspin to identify mononuclear cells, neutrophils and lymphocytes using an optical microscope (Olympus BH2, Olympus Optical Company Ltd, Tokyo, Japan). A non-parametric one-way analysis of variance (ANOVA) with a post-hoc Tukey-type test (28) was conducted to examine the effect of doses compared with the matched control using Origin version 8 (Northampton, MA, USA). Two-way ANOVA was conducted that examined the effect of particle and dose for the three post-exposure time points. Data were analysed using the R statistical computing environment (29). The model assumptions for normality and the constant variance assumption were tested using the Anderson–Darling statistic for normality (30) and the Leven’s test for homogeneity of variance (31). However, these assumptions were not satisfied. As a result, the analysis was conducted on the ranks. As the interaction term was significant ($P < 0.0001$), the post hoc analysis was conducted on the pairwise comparisons. The Holm–Sidak procedure (32) was used to adjust the P values for multiple testing. The estimate and standard error was reported using the untransformed data.

Cellular toxicity assays

Cell-free BALF supernatants were assessed for evidence of lung injury at 1- and 90-day post-exposure time points.

β-N-Acetylglucosaminidase activity assay

Commercially available β-N-acetylglucosaminidase (NAG) activity colorimetric assay kit (Biovision, CA, USA) was used according to the manufacturer’s instructions. In this assay, 125 µL standard

synthetic *p*-nitrophenol derivative (*p*NP) or BALF were incubated for 30 min at 37°C in the presence of NAG substrate, when the reaction was terminated by adding a stop solution. The release of *p*NP was determined by measuring the absorbance at 400 nm.

Alkaline phosphatase activity assay

Commercially available alkaline phosphatase (ALP) activity fluorometric assay kit (Biovision, CA, USA) was used according to the manufacturer’s instructions. Briefly, 120 µL BALF or standard ALP enzymes were incubated with 4-methylumbelliferyl phosphate disodium salt (MUP) for 30 min at room temperature, when the reaction was terminated by adding a stop solution. The fluorescence was measured at Ex/Em = 360nm/440nm using a fluorescence microtitre plate reader.

TEM of lung tissues

TEM analysis of lung tissues was conducted through the services available at the Electron Microscopy Core Laboratory, Cell Imaging and Histology Core Facility, University of Ottawa Heart Institute, Ottawa, Canada. In brief, lung tissues from control and TiO₂NP exposed (two mice/group) mice collected on Days 1, 28 or 90 post-exposure time points were perfused and fixed with 2.5 % glutaraldehyde (electron microscopy sciences, Hatfield, PA, USA) and 2% paraformaldehyde solution (electron microscopy sciences, Hatfield, PA, USA). The fixed lung tissue samples were cut into small pieces, rinsed with 0.15M phosphate buffer and 0.15M sodium cacodylate buffer, post-fixed in 2 % osmium tetroxide (Polysciences, Inc., Warrington, PA, USA) and 0.05M potassium ferricyanide (Sigma–Aldrich Canada Ltd., Oakville, ON, Canada) in 0.12M sodium cacodylate buffer (pH 7.2) for 2h. The osmofication was followed by three rinses with Milli-Q and en bloc staining with 1% uranyl acetate (Leica Microsystems, Ultrastain-1, Buffalo Grove, IL, USA) in Milli-Q water overnight at 4°C. The samples were gradually dehydrated in ethanol on the following day and embedded in Epon according to the standard procedures (TAAB Laboratories Equipment, TAAB 812 resin kit, West Berkshire, UK). Embedded samples were ultrathin-sectioned on a Leica EM UC6 ultramicrotome (Leica Microsystems GmbH, Wetzlar, Germany). The resulting sections

were stained with uranyl acetate and lead citrate before they were visualised using TEM.

Total RNA extraction and purification

Total RNA was isolated from random sections of the left lung lobe ($n = 5$ per experimental group) using TRIzol reagent (Invitrogen, Carlsbad, CA, USA) and purified using RNeasy Plus Mini kits (Qiagen, Mississauga, ON, Canada) according to the manufacturer's instructions. Total RNA concentration was measured using a NanoDrop 2000 spectrophotometer (Thermo Fisher Scientific Inc., Wilmington, DE, USA), and RNA quality and integrity was assessed using an Agilent 2100 Bioanalyzer (Agilent Technologies, Inc., Mississauga, ON, Canada) according to the manufacturer's instructions. All samples showed RNA integrity numbers above seven.

Microarray hybridization

Total RNA (250 ng) samples from individual mice ($n = 5$ per experimental and control group) and from Universal Mouse Reference total RNA (UMRR; Agilent Technologies, Inc., Mississauga, ON, Canada) were used to synthesise double-stranded complementary DNA (cDNA), which was then used to synthesise Cyanine-labelled cRNAs using Quick Amp Labeling Kit (Agilent Technologies Inc., Mississauga, ON, Canada) according to the manufacturer's instructions. cRNAs from experimental (control and TiO₂NPs-exposed) groups were labelled with cyanine 5-CTP and reference cRNAs were labelled with cyanine 3-CTP using a T7 RNA polymerase *in vitro* transcription kit (Agilent Technologies Inc., Mississauga, ON, Canada) and purified using RNeasy Mini kits (Qiagen, Mississauga, ON, Canada). An equimolar amount of reference cRNA was mixed with each experimental cRNA sample and was hybridised to Agilent mouse 4 × 44k oligonucleotide microarrays (Agilent Technologies Inc., Mississauga, ON, Canada) for 17 h in a hybridisation chamber at 65°C with a rotation speed of 10 rpm. At the end of hybridization, arrays were scanned on an Agilent G2505B scanner according to manufacturer's protocols (Agilent Technologies Inc., Mississauga, ON, Canada). Gene expression data from the scanned images were extracted using Agilent Feature Extraction software version 9.5.3.1.

Statistical analysis of microarray data

A reference randomised block design (33) was used to analyse microarray data, normalised using LOcally WEighted Scatterplot Smoothing (LOWESS) regression modelling method and statistical significance of the differentially expressed genes was determined using MicroArray ANalysis Of VAriance (MAANOVA) in R statistical software (<http://www.r-project.org>). The Fs statistic (34) was used to test the treatment effects compared with the matched controls exposed to vehicle only and P values were estimated by the permutation method using residual shuffling. In order to minimise any false positives, the false discovery rate (FDR) multiple testing correction (35) was applied. The fold changes of gene expression were calculated considering the least square means. Genes showing expression changes of at least 1.5-fold in either direction compared with their matched controls and showing FDR $P \leq 0.05$ were considered as significantly differentially expressed genes (DEGs) and were used in all downstream analyses. All microarray data have been deposited in the NCBI gene expression omnibus database and can be accessed via the accession number GSE81570.

Functional and pathway analysis of DEGs

Functional gene ontology (GO) analysis of the DEGs was performed using the Database for Annotation, Visualization and Integrated Discovery (DAVID) v6.7. Benjamini–Hochberg-corrected GO processes, with a Fisher's exact $P \leq 0.05$ considered to be significantly enriched (over-represented). Specific biological pathways associated with the DEGs were identified using Ingenuity Pathway Analysis (IPA, Ingenuity Systems, Redwood City, CA, USA). Pathways with a Fisher's exact P value of ≤ 0.05 were considered for the interpretation of results.

All DEGs from the highest dose of 486 µg/mouse groups were mined against the genomic data repositories in NextBio (<http://ehsr.nextbio.com>) to identify curated studies of diseases with similar gene profiles, gene ranking and consistency in fold change directionality. Pairwise gene signature correlations and rank-based enrichment statistics were employed to calculate the NextBio scores for each disease. The disease (associated with TiO₂NPs exposure) that ranked the highest was given a score of 100 and the rest were normalised accordingly. The meta-analysis function in NextBio was used to compare the DEGs associated with most enriched GOs from TiO₂NP-exposed lung to those reflective of lung fibrosis from the curated datasets available in NextBio.

Histopathology

For histopathology examinations, whole lungs from control and TiO₂NP-exposed mice ($n = 3$) were perfused and fixed in 10% formalin, dehydrated with graded alcohol and paraffin embedded prior to staining with H & E. Three mice per dose group per particle type for a total of 90 slides at each post-exposure time point were assessed. Lung sections from the 162 and 486 µg/mouse dose groups were also stained with Masson trichrome stain to assess collagen deposition. The service was carried out in the PALM Histology Core Facility, University of Ottawa, Ottawa, Ontario, Canada.

Results

Since the 18 µg/animal dose showed non-significant changes in the BALF inflammatory cell profile as measured by the BALF differential cell counts and since it did not induce any observable cellular toxicity as measured by the NAG or ALP assays, this dose group was not included in the microarray experiments and is not discussed in the Results section below.

Characterization of TiO₂NPs

TEM analysis

The primary particle size and morphology of ^aTiO₂⁸, ^aTiO₂²⁰, ^aTiO₂³⁰⁰, ^{ra}TiO₂²⁰, ^rTiO₂²⁰ (HY) and ^rTiO₂²⁰ (HP) were determined by TEM analysis. The average diameter of the majority of each particle type obtained from TEM analysis showed values close to those reported by the manufacturer, except for ^aTiO₂³⁰⁰ (Table 1). Some differences in sizes and particle shapes were observed. Whereas ^aTiO₂⁸, ^{ra}TiO₂²⁰ and ^aTiO₂³⁰⁰ were spherical in shape, the other TiO₂NPs appeared elongated. The diameter of the cross sections ranged from 18 nm to 52 nm for the ^{ra}TiO₂²⁰ and ^rTiO₂²⁰ (HY). The diameters of the elongated or rod shaped ^aTiO₂²⁰ and ^rTiO₂²⁰ (HP) were ~30 nm and ~35–70 nm, respectively, in the longest cross sections. Diameters of ^aTiO₂³⁰⁰ were much smaller (100–120 nm) than reported by the manufacturer. The size of the ^aTiO₂³⁰⁰ was confirmed using nanoparticle tracking analysis (data not shown) by NanoSight LM20 (NanoSight, Amesbury, UK). All TiO₂NPs were found agglomerated.

DLS analysis

DLS analysis of the particle suspension revealed that all TiO₂NPs agglomerate in water. The number-weighted particle aggregate sizes are presented in Table 1. In suspended form, the ^rTiO₂²⁰ (HP) had the smallest particle aggregate size of 39.3 ± 7.3 nm compared with 242.9 ± 53.1 nm or 242.9 ± 56.4 nm observed for ^aTiO₂²⁰ and ^rTiO₂²⁰, respectively. The number-weighted particle sizes for ^aTiO₂⁸, ^aTiO₂³⁰⁰ and ^rTiO₂²⁰ (HY) were 148.4 ± 38.3, 130.1 ± 49.8 nm and 110.1 ± 27.9, respectively.

Post-exposure detection of TiO₂NPs in lung tissues

TEM analysis was used to detect TiO₂NPs in the ultrastructures of the lung tissues collected on Day 1 and Day 28 post-exposure. TEM images of vehicle only-exposed lung tissues did not reveal any particles on Day 1 (Supplementary Figure 1A-a and A-b) or on Day 28 (Supplementary Figure 1B-a and B-b) post-exposure. In general, all TiO₂NPs were found mostly in an agglomerated state in lungs both at Day 1 and Day 28 post-exposure at all the doses tested (Supplementary Figure 1 presents few representative TEM images of lungs exposed to individual TiO₂NP type). The alveolar space (Supplementary Figure 1A-c, A-g and A-k), endothelium and epithelial membranes (Supplementary Figure 1A-d, A-h and A-l), macrophages (Supplementary Figure 1A-e and A-m), lamellar bodies (Supplementary Figure 1A-j), cytoplasm (Supplementary Figure 1A-i and A-n) and caveolin and near collagen fibres (Supplementary Figure 1A-f) were some of the structures of lungs where TiO₂NPs were found on Day 1 post-exposure.

TiO₂NPs were mainly observed in alveolar space near the microvilli (Supplementary Figure 1B-c, B-f, B-k), within the microvilli (Supplementary Figure 1B-d, B-f and B-n) and inside the vesicles (Supplementary Figure 1B-e, B-l and B-m), in samples collected on Day 28 post-exposure. At this time point, particles were mostly found in a non-agglomerated state suggesting that over time, the larger agglomerates may be breaking down.

BALF cellularity

Differential cell counts.

BALF from five mice from each control and exposed groups was assessed for differential cell counts. Details of the total and differential cell counts are summarised in Figure 2 and in Supplementary Table 1. As such, no general trend in increase in total cell number was observed; however, a non-significant dose-dependent increase in the total number of cells in BALF was observed on Day 1 post-exposure for ^rTiO₂²⁰ NPs (Figure 2A). On Day 28 post-exposure, only the rutile/anatase and rutile groups showed increased number of BALF cells at the high dose (Figure 2B).

The mononuclear cells, neutrophils and lymphocytes accounted for 98–99.7%, 0.3–1.8% and ~1.0% of the total cell population of control BALF, respectively. According to the cellular profiles shown in Figure 2A, a dose-dependent decrease in the number of mononuclear cells (Figure 2A-b) and concomitant increase in the number of neutrophils (Figure 2A-c) was observed at Day 1 post-exposure, regardless of the type of TiO₂NPs. The highest increase in neutrophils was observed in mouse lungs exposed to ^rTiO₂²⁰ (HP) (Supplementary Table 1 and Figure 2A-c). The changes in the number of lymphocytes at any dose were not significant (Figure 2A-d).

The changes in the number of mononuclear cells following exposure to rutile/anatase or rutile NPs were observed but not for the anatase NPs on Day 28 post-exposure (Figure 2B-b); a dramatic decrease in the number of BALF neutrophils was observed for all

groups (Figure 2B-c). Moreover, a dose-dependent increase in the total number of lymphocytes was observed for all TiO₂NP groups on Day 28 post-exposure; although only the changes at medium and high doses were significant (Figure 2B-d).

Microarray analysis

Gene expression analysis

Global lung gene expression profiles derived from a total of 240 microarrays were used to assemble the data. Two main comparisons were made: (i) ^aTiO₂⁸, ^aTiO₂²⁰ and ^aTiO₂³⁰⁰ were compared to understand size-related effects and (ii) ^rTiO₂²⁰, ^rTiO₂²⁰ (HY) and ^rTiO₂²⁰ (HP) were compared to understand the influence of surface modification. Each individual data set was analysed separately to identify the specific changes in gene expression compared with the matched vehicle controls. A list of all DEGs (upregulated and downregulated genes) on Day 1 and Day 28 following exposure to six individual types of TiO₂NPs are presented in Supplementary Table 2. Figure 3A summarises the number of upregulated and downregulated genes for all doses and post-exposure time points for each particle type.

Gene expression changes induced by the anatase type of TiO₂NPs

A total of 225, 105 and 85 unique DEGs (Figure 3A, Supplementary Table 3a–c). The DEGs that were common to more than one dose were only counted once.) were found in the lungs of mice exposed to ^aTiO₂⁸, ^aTiO₂²⁰ and ^aTiO₂³⁰⁰, respectively, on Day 1 post-exposure time point. Specific to individual dose groups, ^aTiO₂⁸ did not have any DEGs at the low (54 µg) dose; whereas 8 (all upregulated) and 224 (185 genes upregulated and 39 downregulated) DEGs were found in the 162 and 486 µg dose groups, respectively. The most DEGs were mainly associated with the inflammatory and acute phase signalling pathways. The large fold changes were observed for members of the Serum amyloid A (*Saa*); *Saa3* (38.0-fold), *Saa2* (3.4-fold) and *Saa1* (8.9-fold). The others included tissue inhibitor of metalloproteinase 1 (*Timp1*, 10.1-fold), chemokine (C–C motif) ligand (Ccl) 2 (*Ccl2*, 6.3-fold), *Ccl7* (6.8 fold), lipocalin 2 (*Lcn2*, 5.1-fold), chemokine (C–X–C motif) ligand (*Cxcl1*) 1 (*Cxcl1*, 4.0-fold), *Cxcl10* (3.8-fold) and *Cxcl5* (3.6-fold). Fewer DEGs were observed for the ^aTiO₂²⁰ type at all doses and post-exposure time points; a total of 4, 4 and 72 upregulated and 0, 0 and 30 downregulated DEGs in the 54, 162 and 486 µg dose groups were observed, respectively, at Day 1 post-exposure. *Saa3* (79.6-fold), *Saa1* (10.1-fold), *Timp1* (11.7-fold), *Ccl2* (4.7-fold) and *Lcn2* (9.0-fold) were significantly differentially expressed for ^aTiO₂²⁰. The lungs of mice exposed to ^aTiO₂³⁰⁰ showed a total of 85 unique genes differentially expressed. Among these 4, 6 and 69 DEGs were upregulated and 2, 0 and 12 were downregulated in 54, 162 and 486 µg dose groups, respectively. A large number of inflammation-associated genes including, *Saa3* (71.2-fold), *Saa2* (4.3-fold), *Saa1* (8.4-fold), *Timp1* (6.6-fold), *Ccl2* (2.8-fold), *Ccl7* (2.8-fold), *Ccl17* (2.6-fold), *Lcn2* (8.7-fold), *Cxcl1* (2.1-fold), *Cxcl10* (1.9-fold) and *Cxcl5* (3.4-fold) were significantly expressed in mouse lungs exposed to ^aTiO₂³⁰⁰ at the highest dose.

At Day 28, the response was largely reversed for all three particle types. A total of 8, 5 and 25 DEGs were (Figure 3A, Supplementary Table 3d–f) found in the lungs of mice exposed to ^aTiO₂⁸, ^aTiO₂²⁰ and ^aTiO₂³⁰⁰, respectively, at Day 28 post-exposure. The ^aTiO₂⁸ group showed 2 (upregulated) and 8 (3 upregulated and 5 downregulated) DEGs in the 162 µg and 486 µg dose groups, respectively. The ^aTiO₂²⁰ NPs induced differential expression of 5 (3 upregulated and

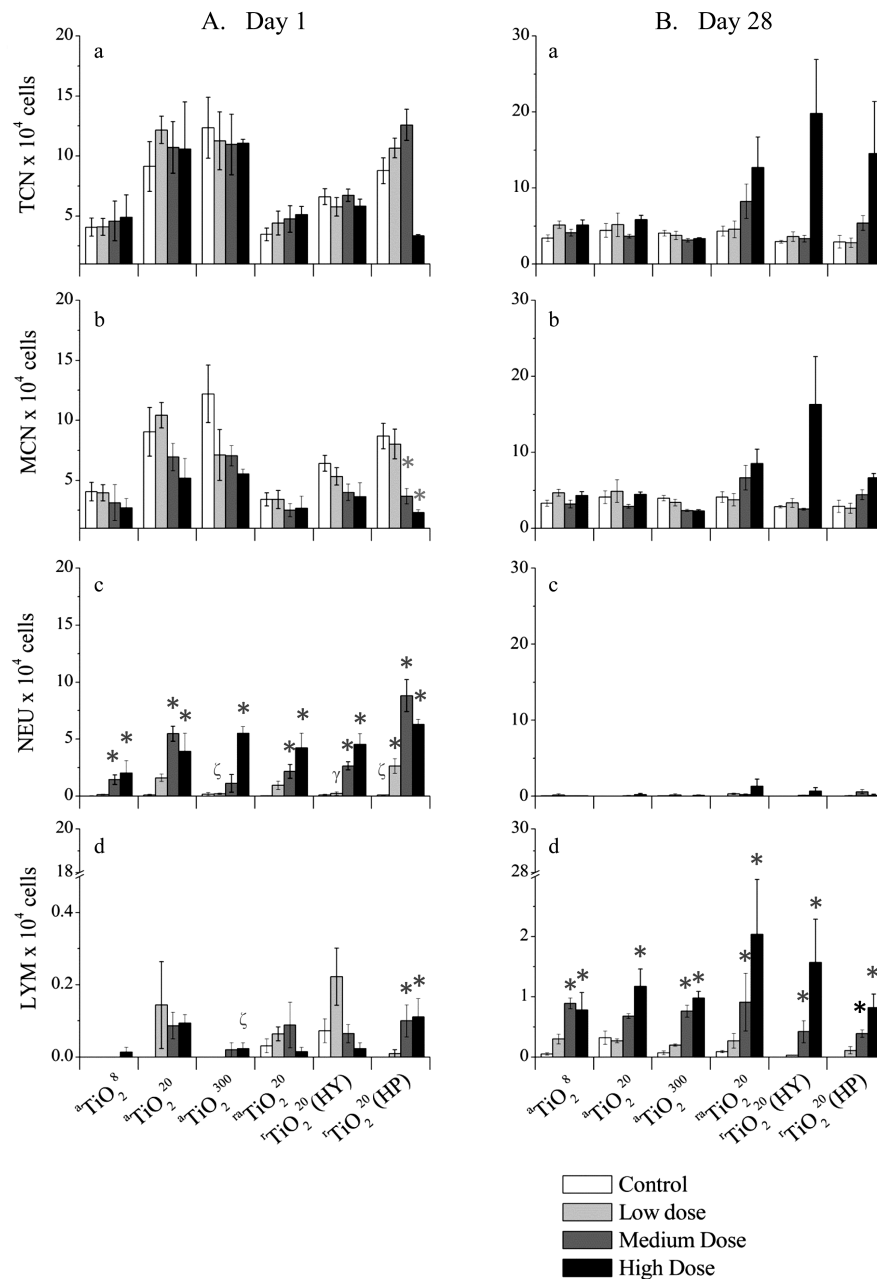


Figure 2. Differential cell counts in BALF fluid on (A) Day 1 post-exposure and (B) Day 28 post-exposure. TCN, MCN, NEU and LYM represent total cell count, monocytes, neutrophils and lymphocytes, respectively. * $P \leq 0.05$: Significant compared with the matched controls by a non-parametric one-way ANOVA with a post-hoc Tukey-type experimental comparison test. A pairwise comparison was performed using post-hoc test following a significant interaction that examined the effects of particle and dose for the two post-exposure time points. † $P \leq 0.05$: Significant compared with $^a\text{TiO}_2^8$; ‡ $P \leq 0.05$: Significant compared with $^r\text{TiO}_2^{20}$ (HY).

2 downregulated) and 3 (2 upregulated and 1 downregulated) genes in each of the 54 and 486 μg dose groups, respectively, and none in the 162 μg dose group. *Nr1d1* (2-fold), *Spon2* (-2.1-fold) and *Nr1d1* (1.9-fold) genes associated with inflammation were altered following exposure to $^a\text{TiO}_2^8$ and $^a\text{TiO}_2^{20}$, respectively. In the mice treated with $^a\text{TiO}_2^{300}$, 1, 4 and 12 DEGs were upregulated and 4, 7 and 11 genes were downregulated in the 54 μg , 162 μg and 486 μg dose groups, respectively. *Myl9* (1.6-fold) associated with muscle contractile activity and *Hspa1a* (-1.8-fold) and *KFL4/KFL9* (-1.8-fold) genes associated with carcinoma were significantly perturbed following $^a\text{TiO}_2^{300}$ exposure; none of the DEGs in the $^a\text{TiO}_2^{300}$ -exposed lungs was associated with inflammation.

Gene expression changes induced by the rutile type of TiO_2 NPs

In contrast to the anatase type TiO_2 NPs described above, the transcriptomic responses to rutile type $^r\text{TiO}_2^{20}$, $^r\text{TiO}_2^{20}$ (HY) and $^r\text{TiO}_2^{20}$ (HP) were robust. A total of 719, 104 and 354 genes were (Supplementary Table 3g-i) differentially expressed in the lungs of mice exposed to $^r\text{TiO}_2^{20}$, $^r\text{TiO}_2^{20}$ (HY) and $^r\text{TiO}_2^{20}$ (HP), respectively, on Day 1 post-exposure. The mixed unmodified $^r\text{TiO}_2^{20}$ -induced 33 DEGs (31 upregulated and 2 downregulated) in the 54 μg , 108 DEGs (84 upregulated and 24 downregulated) in the 162 μg and 714 DEGs (401 upregulated and 313 downregulated) in the 486 μg dose groups (Supplementary Table 3g-i). The $^r\text{TiO}_2^{20}$ (HY) modified

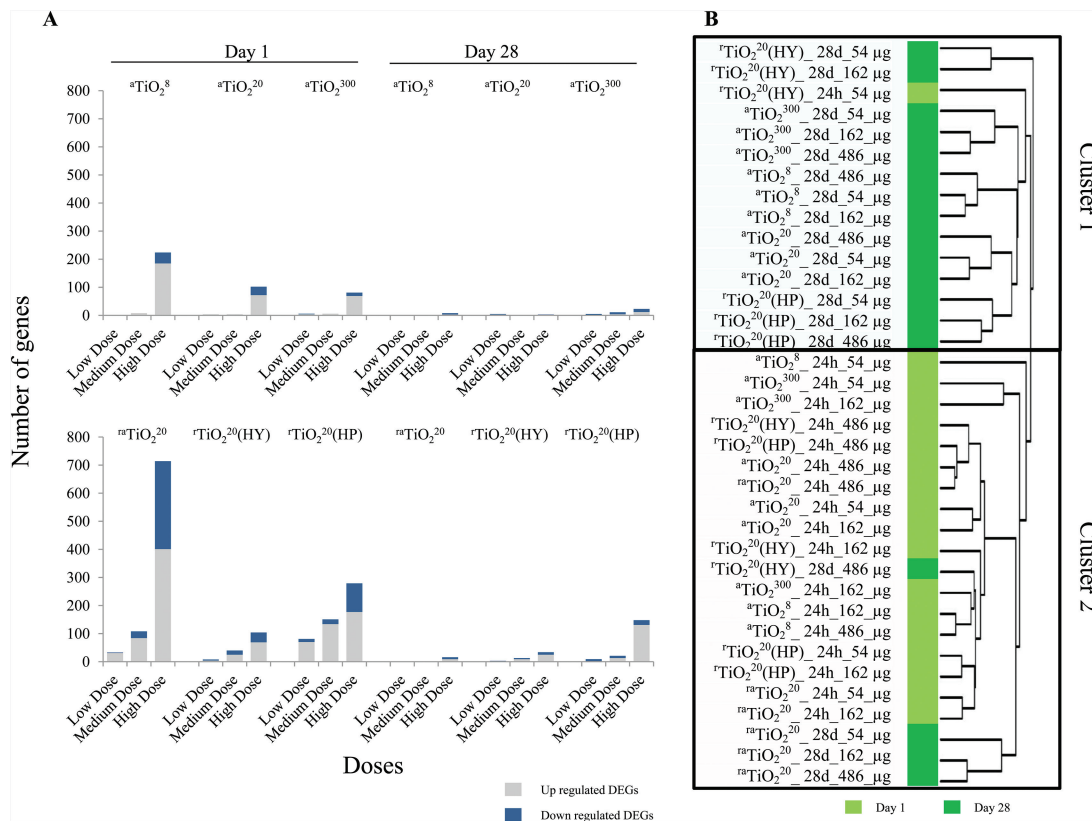


Figure 3. (A) Differentially expressed genes (FDR P value ≤ 0.05) following exposure to TiO_2 NPs on Day 1 and on Day 28. (B) Hierarchical clustering.

with aluminum oxide and dimethicone induced fewer DEGs compared with $^{\text{r}}\text{TiO}_2^{20}$ and $^{\text{r}}\text{TiO}_2^{20}$ (HP) at all the doses tested; 4, 25 and 69 genes were upregulated and 4, 15 and 35 genes were downregulated for the 54 μg , 162 μg and 486 μg dose groups (Supplementary Table 3g–i). In comparison, the $^{\text{r}}\text{TiO}_2^{20}$ (HP) modified with aluminum oxide and glycerol induced significantly higher number of DEGs at all three doses and post-exposure time points; a total of 70, 134 and 177 genes were upregulated and 11, 17 and 102 DEGs were downregulated on Day 1 post-exposure in the 54 μg , 162 μg and 486 μg dose groups, respectively.

At the highest dose, the genes associated with inflammation including, *Saa3* (64.5, 41.6, 87.6-fold), *Saa2* (5.6, 5.1, 5.4-fold), *Saa1* (13.0, 5.2, 11-fold), *Ccl7* (4, 4, 6.2 fold), *Ccl17* (3.5, 3.5, 3-fold), *Lcn2* (9.3, 5.9, 8.5-fold) and *Cxcl1* (2.2, 3.8, 3.2-fold) showed the highest fold changes following exposure to $^{\text{r}}\text{TiO}_2^{20}$, $^{\text{r}}\text{TiO}_2^{20}$ (HY) or $^{\text{r}}\text{TiO}_2^{20}$ (HP), respectively. The *Ccl2* (6.3-fold) showed significant fold change following exposure to $^{\text{r}}\text{TiO}_2^{20}$ (HP) only. In addition, the expression of interleukin 1 receptor, type II (*Il1r2*, 3.3, 2.7-fold), (*Il1B*, 1.9, 2.2-fold), cytochrome P450 family 7 subfamily B member 1 (*Cyp7b1*, 3.3, 3.4-fold) and placenta growth factor (*Pgf*, 2.2, 2.0-fold) responsible for fibrosis were also upregulated following exposure to $^{\text{r}}\text{TiO}_2^{20}$ and $^{\text{r}}\text{TiO}_2^{20}$ (HP), respectively, and *Timp1* (19.8, 5.5, 12.7-fold) and Cd14 antigen, (*Cd14*—1.9, 1.8, 2.3-fold) were differentially expressed in all three rutile groups, $^{\text{r}}\text{TiO}_2^{20}$ and $^{\text{r}}\text{TiO}_2^{20}$ (HP) and $^{\text{r}}\text{TiO}_2^{20}$ (HY). Serine (or cysteine) peptidase inhibitor, clade E, member 1, (*Serpine1*, 2.6-fold) was upregulated only in the $^{\text{r}}\text{TiO}_2^{20}$ group.

Fewer genes were altered at Day 28 post-exposure to $^{\text{r}}\text{TiO}_2^{20}$ (Supplementary Table 3j); none in the 54 μg dose group, and 1 upregulated and 1 DEGs downregulated in the 162 μg group. In the 486 μg group, 9 were upregulated and 7 DEGs were downregulated.

Ly6f (2.8-fold), *Trem2* (2.2-fold), *Nr1d2* (1.9-fold) and *Spon2* (–2.3-fold) were among the genes differentially expressed at the highest dose that were associated with inflammation. Several genes were persistently altered at Day 28 following exposure to $^{\text{r}}\text{TiO}_2^{20}$ (HY) (Supplementary Table 3k); 3 (1 upregulated, 2 downregulated), 13 (9 upregulated, 4 downregulated) and 34 (25 upregulated, 9 downregulated) genes showed differential expression in the 54, 162 and 486 μg groups, respectively. In response to $^{\text{r}}\text{TiO}_2^{20}$ (HP), 9 (2 upregulated and 7 downregulated), 21 (13 upregulated and 8 downregulated) and 148 (131 upregulated and 17 downregulated) DEGs were found in the 54, 162 and 486 μg dose groups, respectively (Supplementary Table 3l). Several genes associated with inflammation and acute phase signalling were persistently altered at Day 28 following exposure to $^{\text{r}}\text{TiO}_2^{20}$ (HY) and $^{\text{r}}\text{TiO}_2^{20}$ (HP). These included *Saa3* (27.7 and 7.0-fold), *Lcn2* (7.9 and 6.3-fold), *Cxcl5* (5.4 and 5.7-fold), *Ccl7* (4.0 and 5.0-fold), *Cxcl1* (3.6 and 2.6-fold), *Clec5a* (2.5 and 2.5-fold) and *Cd14* (2.1 and 1.8-fold), respectively, at the high dose. In addition, pro-fibrotic genes including *Cd14* (2.1-fold), *Timp1* (2.5-fold) and *Cyp7b1* (2.2-fold) following $^{\text{r}}\text{TiO}_2^{20}$ (HY) and *Ccl2* (4.1-fold), *Csf2* (2.1-fold), *Cd14* (1.8-fold), *Adora1* (1.7-fold) and *Il1rn* (1.5-fold) following $^{\text{r}}\text{TiO}_2^{20}$ (HP) showed largest changes at the high dose.

In addition to a separate assessment of the individual data sets, a hierarchical clustering of genes differentially expressed in at least one experimental condition was conducted to determine particle, dose, or time-dependent expression patterns (Figure 3B). The analysis revealed that the expression patterns were similar for individual mice within the same treatment groups. Two main clusters were observed: Cluster-1 consisted of all doses of the five TiO_2 NPs for Day 28 post-exposure time point excluding $^{\text{r}}\text{TiO}_2^{20}$, along with

Day 1 post-exposure samples of rTiO_2^{20} (HY) from the low-dose group. The Cluster-2 included Day 1 samples of all six TiO_2 NP types along with Day 28 post-exposure samples of rTiO_2^{20} from all dose groups and Day 28 post-exposure samples of rTiO_2^{20} (HY) from the high-dose group. The results suggested that the observed responses at the gene expression level were mainly post-exposure time-dependent and particle-specific differences were not observed (Figure 3B).

Influence of size on gene expression

Size-related effects were assessed by comparing gene expression responses to aTiO_2^8 , aTiO_2^{20} and aTiO_2^{300} ; Supplementary Table 3a–f lists DEGs from this group of samples. In general, the number of DEGs at Day 1 post-exposure was remarkably lower for the aTiO_2^{300} exhibiting surface area of $10 \text{ m}^2/\text{g}$ (85 genes) and was highest for the aTiO_2^8 exhibiting surface area of $229\text{--}235 \text{ m}^2/\text{g}$ (225 genes) among all dose groups. In comparison, the aTiO_2^{20} with the surface area of $90 \text{ m}^2/\text{g}$ showed 105 DEGs. A VENN analysis of all DEGs from all three anatase types showed that no genes in common in the low-dose group ($54 \mu\text{g}$), and three genes in the $162 \mu\text{g}$ and 7 genes in the $486 \mu\text{g}$ groups (Supplementary Figure 2). The common genes included *Saa3*, *Saa1*, *Timp1*, *Lcn2*, *Ccl2*, and *Bcan*, all of which are associated with the process of lung inflammation. In addition, *Il1r2* a pro-fibrotic gene was common to all (Supplementary Table 3). On Day 28 post-exposure, only one DEG at the highest dose (Supplementary Figure 2B) was common to all anatase groups.

Functional pathway analysis

The DEGs were analysed to identify specific biological functions, processes or pathways perturbed following exposure. In agreement with the total number of DEGs, a large number of perturbed biological processes were observed in the 162 and $486 \mu\text{g}$ dose groups. The list of all biological processes affected at Day 1 post-exposure for all doses are summarised in Supplementary Table 4. Immune/inflammation responses were the top processes affected following exposure to all anatase TiO_2 NPs, with enrichment of GO annotations such as inflammatory response (GO:0006954), response to wounding (GO:0009611), defense response (GO:0006952), chemotaxis (GO:0006935), taxis (GO:0042330) and behaviour (GO:0007610). In addition, genes in the high-dose group of the aTiO_2^{300} also perturbed steroid metabolic process (GO: 0008202). The largest significant changes were observed in mice exposed to aTiO_2^8 . No biological processes were significantly altered in aTiO_2^{20} -exposed lungs. Two biological processes—transcription (GO:0006350) and rhythmic process (GO:0048511)—were altered in aTiO_2^{300} group at Day 28 post-exposure. There were no significantly altered biological processes for the other two anatase types.

The microarray data were further analysed through Kyoto Encyclopedia of Genes and Genomes (KEGG) and Ingenuity Pathway Analysis (IPA) to understand the implications of the altered genes in lung diseases and disorders. The list of all KEGG pathways affected at Day 1 post-exposure is provided in Supplementary Table 4; the cytokine–cytokine receptor interaction (mmu04060), chemokine signalling pathway (mmu04062) and NOD-like receptor signalling (mmu04621) pathways implicated in the inflammation process were among the top pathways affected. In addition, the terpenoid backbone biosynthesis (mmu00900) and p53 signalling pathway (mmu04115) were altered in response to aTiO_2^8 and aTiO_2^{20} , and extracellular matrix (ECM)–receptor interaction (mmu04512) and focal adhesion (mmu04510) were perturbed in response to aTiO_2^8 .

This response was not seen in Day 28 post-exposure samples. A heat map of enriched ($-\log P$ value ≥ 1.3) canonical pathways (IPA) regulated by the DEGs at Day 1 and Day 28 are presented in Figure 4. IPA revealed unique association of DEGs in the high-dose group of aTiO_2^{20} with the p53 signalling pathway and the ataxia telangiectasia mutated signalling pathway, implying DNA damage response. The p53 signalling pathway was among the significantly perturbed KEGG pathways that was associated with DEGs of aTiO_2^{20} and aTiO_2^8 . The DEGs in the high-dose group of aTiO_2^8 and aTiO_2^{300} showed significant association with the pathways of hepatic fibrosis and interleukin 17 signalling in fibroblasts, suggesting a potential for these particles to induce lung fibrosis.

Only a few altered canonical pathways that included acute phase signalling, glucocorticoid receptor signalling and FXR/VDR/LXR/RXR activation were significantly perturbed on Day 28 for all three anatase TiO_2 NPs.

The results showed that the altered DEGs in this group are involved in inflammation, oxidative stress and fibrosis. aTiO_2^8 , aTiO_2^{20} and aTiO_2^{300} induced 24, 12 and 24 DEGs associated with inflammation; 13, 4 and 8 DEGs associated with fibrosis and 2, 7 and 5 DEGs associated with oxidative stress in the $486 \mu\text{g}$ dose group (Supplementary Figure 3). These genes were no longer significantly expressed on Day 28 post-exposure.

Influence of surface modification on gene expression

For the rutile rTiO_2^{20} , rTiO_2^{20} (HY) and rTiO_2^{20} (HP) NPs, transcriptomic response seemed to be influenced by the type of surface modifications. While the rutile/anatase rTiO_2^{20} induced the largest number of DEGs at the high dose on Day 1, rTiO_2^{20} (HP) with hydrophilic surface modification induced large number of DEGs at all doses and post-exposure time points. There were 1, 15 and 36 genes common to rTiO_2^{20} , rTiO_2^{20} (HY) and rTiO_2^{20} (HP) groups at the low, medium and high doses, respectively, which were mainly associated with inflammation (Supplementary Figure 4A). There were 5 and 15 DEGs common to the rTiO_2^{20} (HY) and rTiO_2^{20} (HP) exposure groups, respectively, at the medium and high dose at Day 28 post-exposure. Only 1 and 2 DEGs were common to the three rutile NPs at medium and high doses and none at the low dose (Supplementary Figure 4B).

Functional pathway analysis

The biological processes perturbed on Day 1 and Day 28 post-exposure for all doses are summarised in Supplementary Table 5. Immune/inflammation responses were the top biological processes affected on Day 1 post-exposure, with enrichment of GO annotations, such as inflammatory response (GO:0006954), response to wounding (GO:0009611), defense response (GO:0006952), chemotaxis (GO:0006935), taxis (GO:0042330) and behaviour (GO:0007610) (Supplementary Table 5-a). DEGs in the high-dose group of the rTiO_2^{20} and rTiO_2^{20} (HY) were also associated with steroid metabolic process (GO:0008202). Processes corresponding to cell adhesion were perturbed in the high-dose rTiO_2^{20} group.

At Day 28, significant alterations in the immune/inflammation responses (Supplementary Table 5-b), which were associated with inflammatory response (GO:0006954), response to wounding (GO:0009611), defense response (GO:0006952), chemotaxis (GO:0006935), taxis (GO:0042330) and behaviour (GO:0007610) were seen only in rTiO_2^{20} (HP) group at the highest dose. rTiO_2^{20}

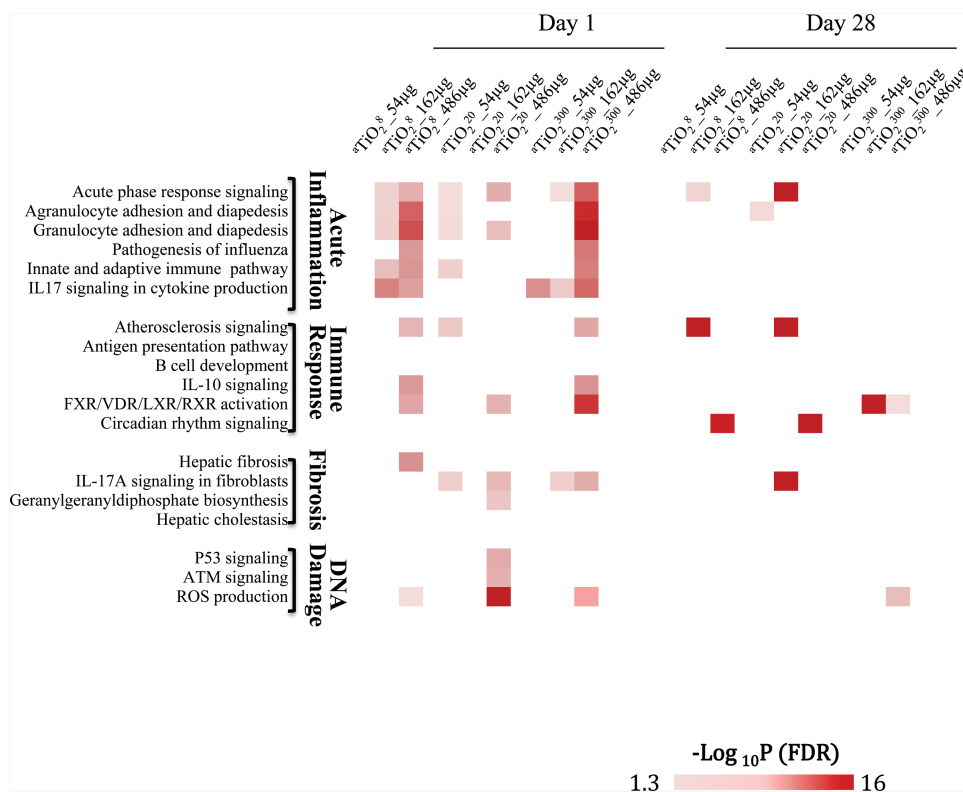


Figure 4. Schematic heat map depicting dose-dependent enrichment in canonical pathways in lungs exposed to ⁸TiO₂, ²⁰TiO₂ or ³⁰⁰TiO₂ at Day 1 and Day 28 post-exposure.

perturbed the alteration of regulation of transcription (GO:0045449), RNA metabolism (GO:0051252), circadian rhythm (GO:0007623) and rhythmic processes (GO:0048511). No significant changes in the biological processes were observed in ²⁰TiO₂ (HY) group at any dose at this late time point.

The list of all KEGG pathways affected at Day 1 and Day 28 post-exposure is provided in [Supplementary Table 5](#); the cytokine-cytokine receptor interaction (mmu04060), chemokine signaling pathway (mmu04062) and NOD-like receptor signalling (mmu04621) pathways implicated in the inflammation process were among the top pathways affected. In addition, the terpenoid backbone biosynthesis (mmu00900), ECM-receptor interaction (mmu04512), focal adhesion (mmu04510) and p53 signalling pathway (mmu04115) were altered in lungs in response to ²⁰TiO₂.

At Day 28 post-exposure, only ²⁰TiO₂ (HP) and ²⁰TiO₂ (HY) showed perturbations in the inflammatory (cytokine-cytokine receptor interaction (mmu04060) and chemokine signalling (mmu04062)) pathways. In addition, ²⁰TiO₂ (HP) showed perturbations in toll-like receptor signalling pathway (mmu04620) and NOD-like receptor signalling (mmu04621) and lysosome (mmu04142) pathways.

Heat map of enriched ($-\log P \geq 1.3$) canonical pathways regulated by the DEGs at Day 1 and Day 28 post-exposure are presented in [Figure 5](#). The top five canonical pathways associated with DEGs on Day 1 include acute phase response signalling, agranulocyte adhesion and diapedesis, granulocyte adhesion and diapedesis, role of hypercytokinemia/hyperchemokinaemia in pathogenesis and communication between innate and adaptive immune cells. In addition to inflammatory pathways, hepatic fibrosis/hepatic stellate cell activation and hepatic cholestasis were perturbed even in the low-dose groups of the rutile ²⁰TiO₂ and ²⁰TiO₂ (HP) and in the medium- and high-dose groups of the ²⁰TiO₂ (HY) at Day 1 post-exposure ([Figure 4](#)).

Altered inflammatory pathways such as acute phase response signalling, agranulocyte adhesion and diapedesis, granulocyte adhesion and diapedesis were also observed at Day 28 post-exposure for all rutile NPs. At this time point, the fibrosis pathway was altered only in the high-dose group of the ²⁰TiO₂ (HY) and ²⁰TiO₂ (HP).

The results also showed that ²⁰TiO₂ induced highest number of DEGs associated with fibrotic (25 DEGs at the high dose) and oxidative stress (14 DEGs at the high dose) response categories on Day 1 ([Supplementary Figure 5](#)); however, these genes were no longer significantly expressed on Day 28 post-exposure. The ²⁰TiO₂ (HY) and ²⁰TiO₂ (HP) induced 6 and 11 DEGs associated with fibrosis on Day 1, respectively. Six of those induced by ²⁰TiO₂ (HY) were also observed on Day 28. Only three DEGs were induced by ²⁰TiO₂ (HP) on Day 28, which were mainly associated with inflammation.

Identification of human diseases associated with perturbed gene expression profiles

Diseases and functions predicted from IPA showed that the diseases and functions related to inflammation were activated in lungs treated with the anatase TiO₂NPs on Day 1 post-exposure ([Supplementary Figure 6](#)). In addition to diseases and functions related to inflammation, diseases and functions related to DNA damage were also activated in lungs treated with ²⁰TiO₂. These diseases and functions were no longer activated on Day 28 post-exposure. In the rutile/anatase and rutile-exposed groups, the diseases and functions related to inflammation, fibrosis and oxidative stress were activated in the 162 μ g and 486 μ g dose groups ([Supplementary Figure 6](#)) on Day 1 post-exposure. These diseases and functions related to inflammation, fibrosis and oxidative stress were only activated in the 486 μ g dose groups on Day 28 post-exposure.

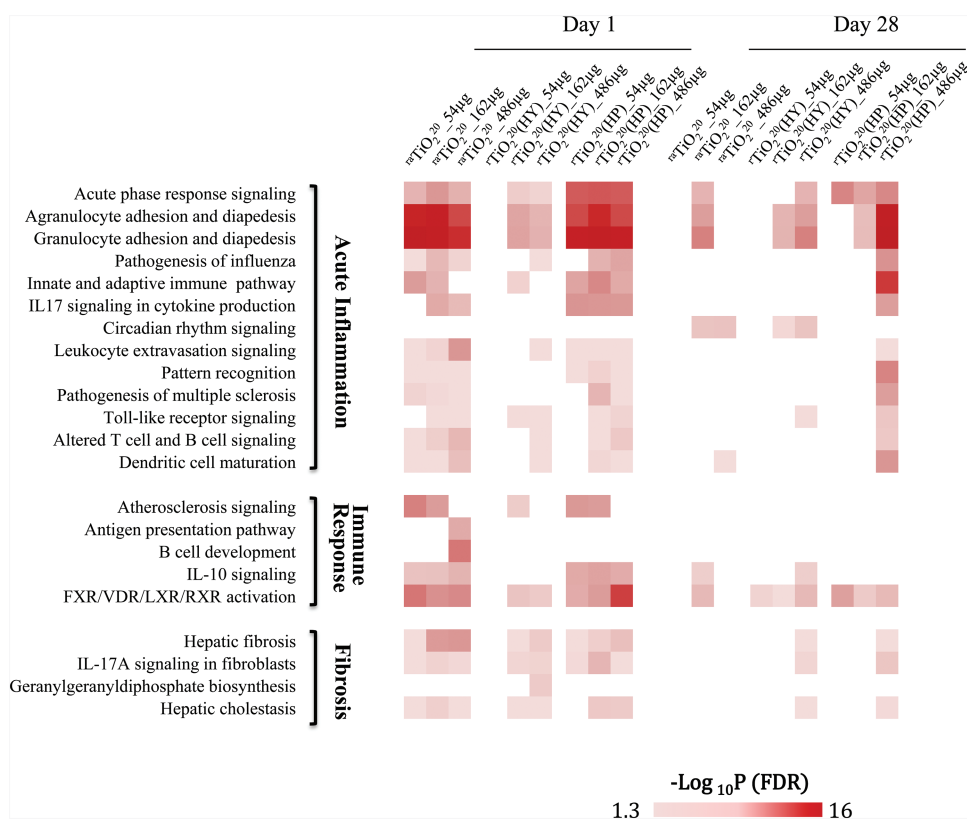


Figure 5. Schematic heat map depicting dose-dependent enrichment in canonical pathways in lungs exposed to $^{a}\text{TiO}_2^{20}$, $^{r}\text{TiO}_2^{20}$ (HY) and $^{h}\text{TiO}_2^{20}$ (HP) at Day 1 and Day 28 post-exposure.

DEGs from the 162 and 486 μg dose groups of all six particle types were analysed using the NextBio Human Atlas (Supplementary Table 6) to identify their potential association with known human diseases. The analysis showed that respiratory disorders, viral infectious diseases, bacterial infectious disease, parasitic disease, and nutritional and metabolic disease are among the top disease categories associated with the DEGs. The sub-categories in the respiratory disorders category included severe acute respiratory syndrome, infectious disease of lung, lower respiratory tract infection, pneumonia, interstitial lung disease, injury of lung, asthma, pulmonary hypertension, chronic obstructive pulmonary disease and fibrosis of lung.

Histopathology

A recently published INHAND system was used to classify lung morphology and lung lesions.⁽³⁶⁾ The H & E-stained slides were blinded for the type of TiO_2 NPs. The detailed lung lesion inventory is provided in Supplementary Table 7. For each lesion category, a numeric score from 0 to 5 was assigned based on a subjective assessment of the lesion severity, which corresponded to lesion not present, minimal, mild, moderate, marked and severe, respectively.

The results showed that lung sections from vehicle-treated control mice on Day 1 post-exposure are well ventilated with a few macrophages distributed diffusely in the alveolar spaces (Figure 6A-a). Infiltration of alveolar macrophages and neutrophils was observed in the treated groups in a dose-dependent manner (Figure 6Ab-m). The alveolar macrophages were heavily laden with NPs. Alveolar inflammation or alveolitis was assessed by the presence of granulomatous and pyogranulomatous like structures dominated by large

numbers of macrophages and neutrophils, respectively. Mild macrophage-neutrophilic alveolitis was also observed in the 162 μg dose group (Figure 6A-b-g). The degree of alveolitis in centriacinar area regions was more prominent in the 486 μg dose group for all particle types (Figure 6A-h-m).

The lung sections remained well ventilated on Day 28 post-exposure (Figure 6B-a). A dose-dependent increase in the alveolar macrophages was observed for some particle types mainly at 162 (Figure 6B-b-g) or 486 μg doses (Figure 6B-n-s); however, this change was less significant compared with the Day 1 post-exposure groups (Supplementary Table 7-b). Peribronchiolar and perivascular infiltrations of lymphocytes were observed in the 162 μg and 486 μg dose groups, except in mice exposed to $^{a}\text{TiO}_2^{300}$ (Supplementary Table 7-b). Focal to multifocal granulomatous and pyogranulomatous inflammation were more pronounced in $^{h}\text{TiO}_2^{20}$ (HY)- and $^{h}\text{TiO}_2^{20}$ (HP)-exposed lungs in the 162 μg (Figure 6B-f-g) and 486 μg dose groups (Figure 6B-r-s). Lung sections were stained with Masson's trichrome staining to assess collagen deposition on Day 28 post-exposure in the medium- and high-dose groups. Masson's trichrome staining showed that collagen depositions were minimal in lung sections treated with TiO_2 NPs in the 162 μg dose groups (Figure 6B-h-m). Collagen depositions were higher in $^{h}\text{TiO}_2^{20}$ (HY)- and $^{h}\text{TiO}_2^{20}$ (HP)-exposed lungs in the 486 μg dose groups (Figure 6B-t-y) compared with other lung sections treated with other TiO_2 NP types.

Long-term effects of exposure to TiO_2 NPs

$^{a}\text{TiO}_2^8$, $^{r}\text{TiO}_2^{20}$, $^{h}\text{TiO}_2^{20}$ (HY) and $^{h}\text{TiO}_2^{20}$ (HP) showed larger transcriptional responses compared with other particle types, suggesting some

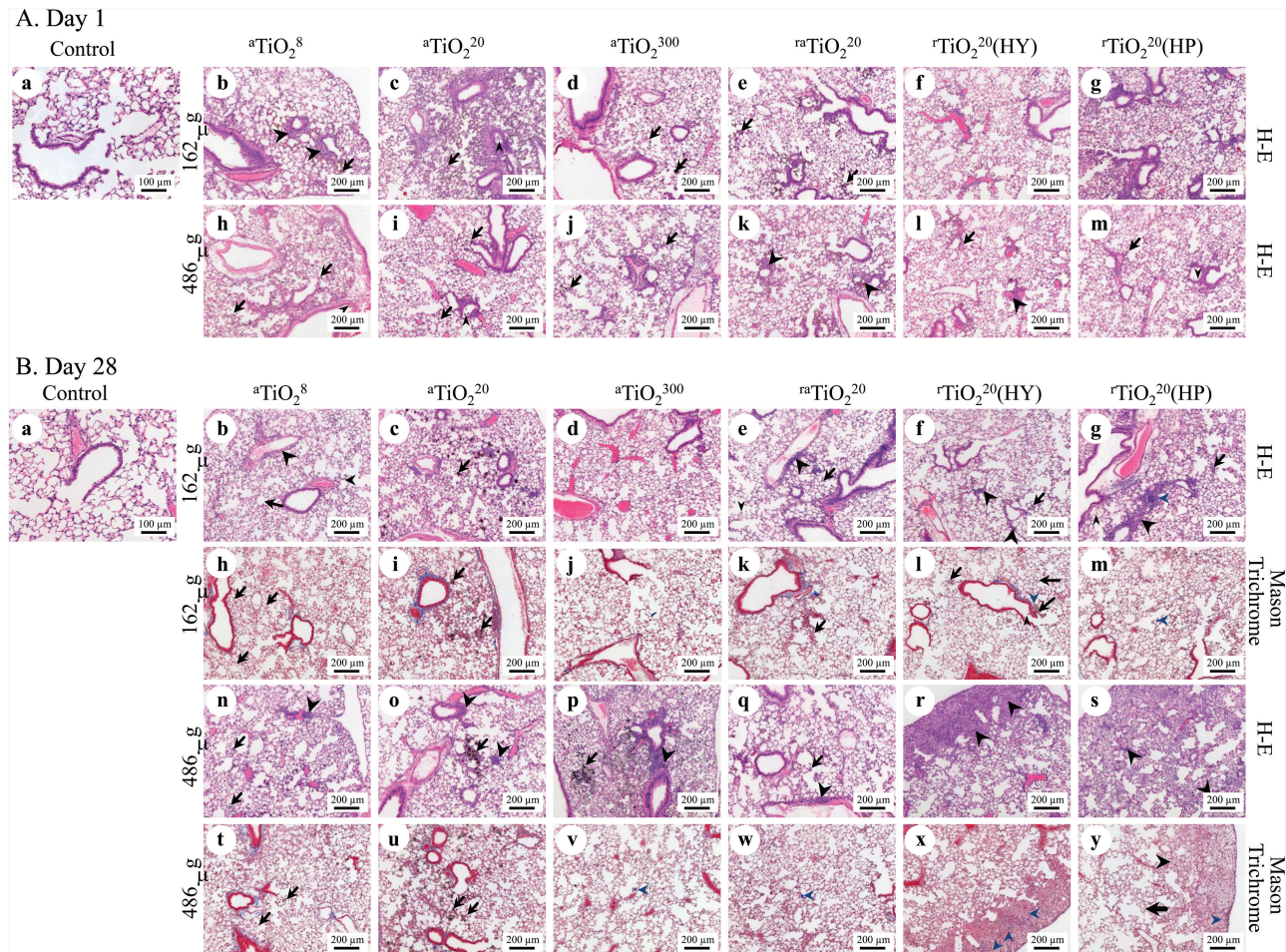


Figure 6. Histopathology of lungs exposed to TiO₂NPs on Day 1 and Day 28 post-exposure. Large arrowhead: infiltration of inflammatory cells; small arrowhead: particle-laden macrophages; arrows: presence of NPs; and blue arrowhead: deposition of collagen associated with fibrosis.

TiO₂NPs may be more harmful than others. Thus, a series of experiments were conducted at 90-day post-exposure to determine whether differential transcriptomics responses among the TiO₂NPs eventually translates into disease manifestation for some TiO₂NPs. TEM analysis of lung sections (Figure 7) showed that an appreciable fraction of TiO₂NPs deposited via single intratracheal instillation were retained in lung tissues up to 90 days post-exposure regardless of the specific size or surface modifications, in the 162 and 486 µg dose groups (Figure 7-a-l). The TiO₂NPs were mostly found dispersed in the cytoplasm and some were localized to phagocytic vacuoles (Figure 7-e-g). In lung sections from the aTiO₂⁸ and rTiO₂²⁰ (HP)-exposed groups, particles were found inside the nuclei (Figure 7-d, 7-l).

BALF cellularity analysis revealed small increases in total cell number (Supplementary Figure 7A-a and B-a), macrophages (Supplementary Figure 7A-b and B-b) and lymphocytes (Supplementary Figure 7A-c and B-c) at 90-day post-exposure, indicating persistent but subtle inflammation. No general trends specific to particle types were observed.

To further understand the nature of the response observed at Day 90 post-exposure, cytotoxicity was assessed using β-NAG activity and ALP activity (37) in cell-free BALF supernatants collected on Day 1 and Day 90 post-exposure. Increased β-NAG activity is indicative of macrophage lysosomal activation (38). Increased ALP activity is used as a marker of (39) pathological pulmonary conditions, in which epithelial damage is a central feature of the pathogenesis,

such as acute lung injury, pulmonary fibrosis, viral pneumonia and particulate matter-induced lung toxicity (40). The results showed that the β-NAG (Supplementary Figure 8A-a and A-b) activity increased significantly on Day 1 following exposure to aTiO₂⁸ and rTiO₂²⁰ (HY) at the medium and high doses and in lungs exposed to rTiO₂²⁰ (HP) at the high-dose group in comparison with their matched controls. The ALP activity (Supplementary Figure 8B-a and B-b) was significantly higher on Day 1 in lungs of mice exposed to aTiO₂⁸ and rTiO₂²⁰ (HP) at the medium and high doses and in lungs exposed to aTiO₂⁸ and rTiO₂²⁰ at the high-dose group compared with their matched controls. The increased β-NAG or ALP activities on Day 1 (Supplementary Figure 8B-a and B-b) were reduced significantly on Day 90.

In alignment with the observations above, the lung sections from the treated animals showed an increased infiltration of alveolar macrophages throughout but particularly in centriacinar area alveolar spaces at 90 Day post-exposure (Figure 8). Perivascular and peribronchiolar infiltrations of inflammatory cells were often observed irrespective of the type of TiO₂NPs (Figure 8). Alveolar or septal fibroblast proliferation and granulomatous alveolar inflammation dominated by macrophages and lymphocytes were observed occasionally in treated lungs. Control mice showed only a subtle and diffuse infiltration of alveolar macrophages (Figure 8A-a-c and B-a-c). Masson's trichrome staining for collagen revealed the presence of mild fibrosis in lungs exposed to aTiO₂⁸ (Figure 8A-j and A-p), rTiO₂²⁰ (HY) (Figure 8B-k and B-q) and rTiO₂²⁰ (HP) (Figure 8B-l and B-r).

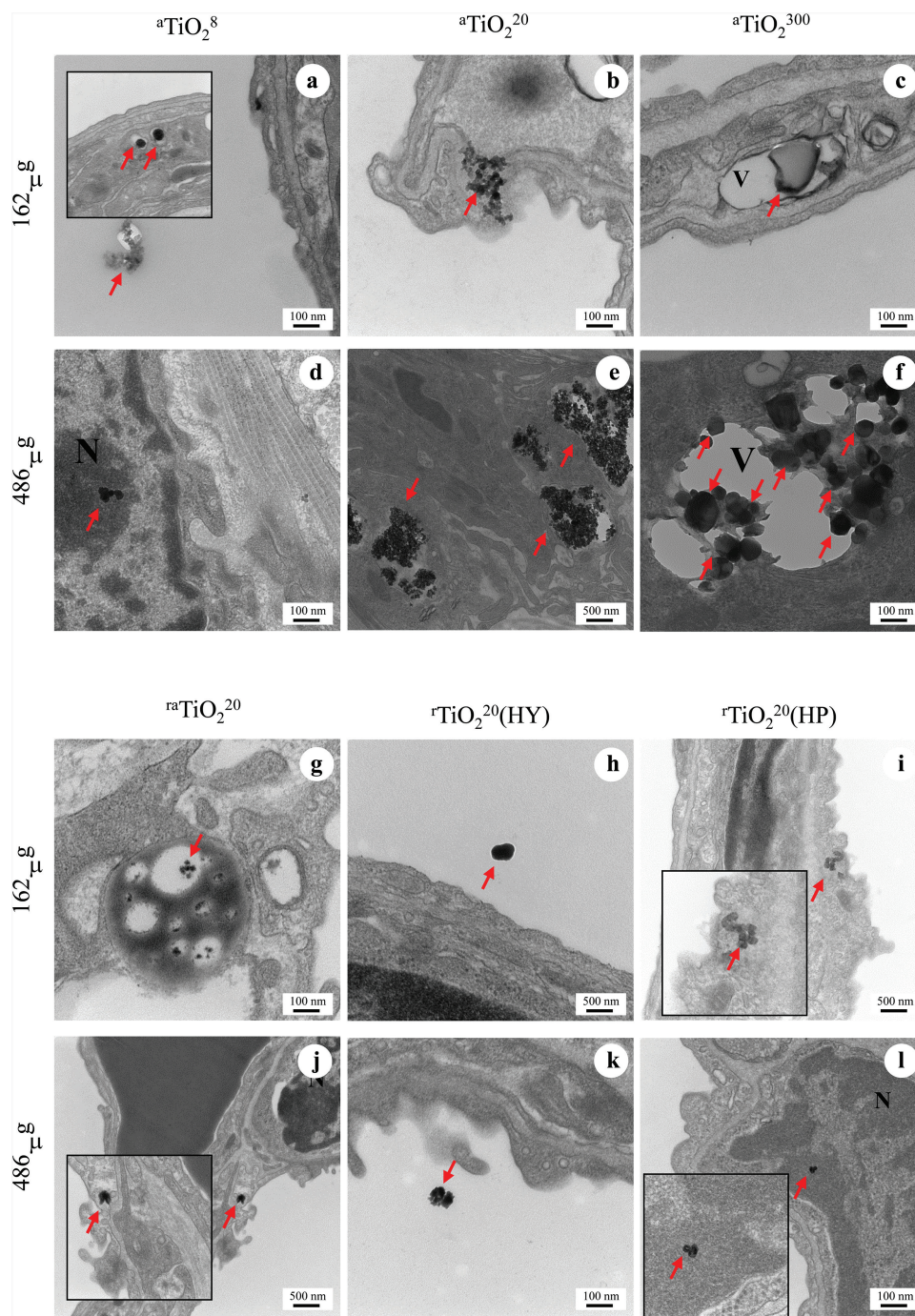


Figure 7. TEM analysis of lung tissue sections on Day 90 post-exposure and detection of TiO_2 NPs in different areas of lungs. Red arrows: presence of NPs; N: nucleus; and V: vacuole.

A mild and focal type 2 pneumocyte hypertrophy and hyperplasia, indicative of repair of alveolar epithelium was found only in lungs exposed to medium dose of $r\text{TiO}_2^{20}$ (HP) (data not shown).

Discussion

Property-specific responses

As stated earlier in the introduction above, it is a well-known fact that the primary particle size and the resulting surface area influence the toxicity induced by several classes of NMs including TiO_2 NPs.

For TiO_2 NP variants, lung exposures leading to acute pulmonary inflammation is suggested to be predominantly dependent on size but also on several other properties such as the surface modifications. However, it is not known whether the underlying mechanisms of pulmonary inflammation are the same for all and it is also not clear whether subtle differences in the severity of acute pulmonary inflammation observed for some TiO_2 NP variants (22) translate into a disease phenotype at a later post-exposure time point. Thus, in the present study, we conducted a detailed assessment of lung responses to six different types of TiO_2 NPs with varying sizes, modifications

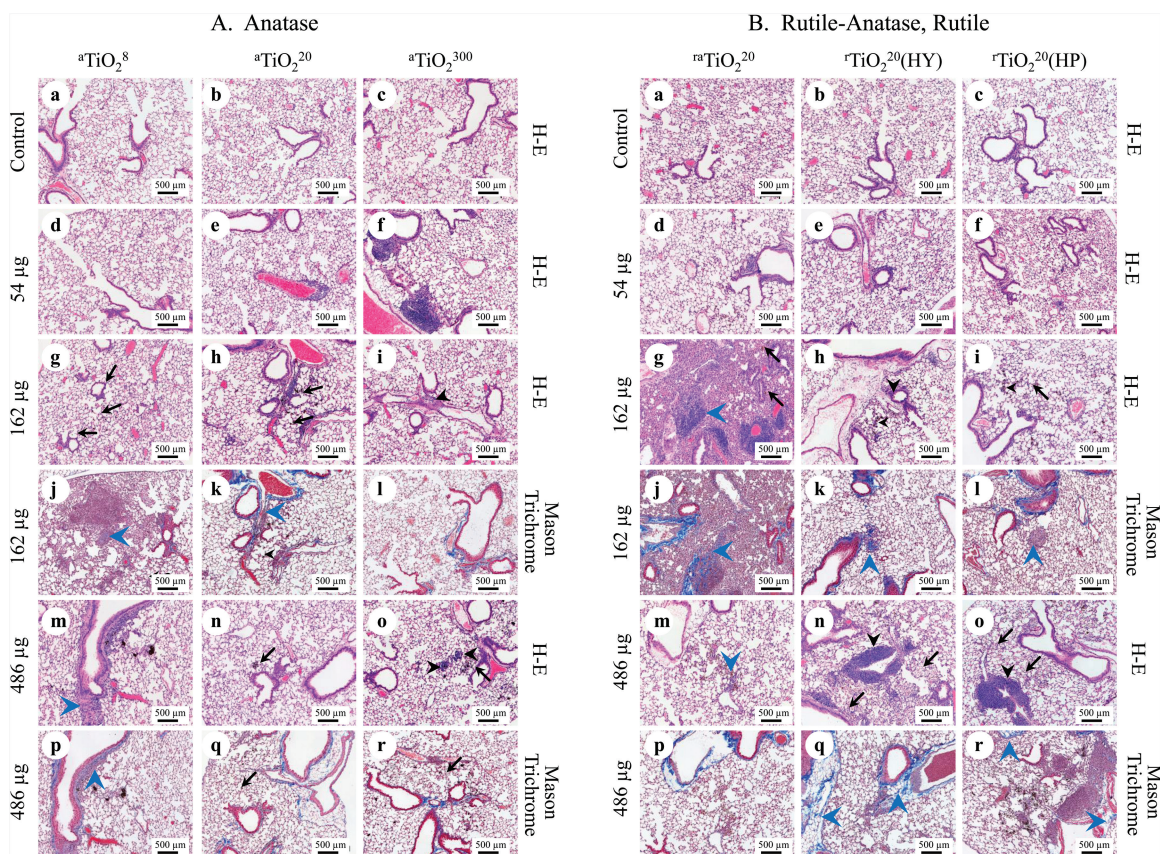


Figure 8. Histopathology of lung tissue exposed to TiO₂NPs on Day 90. Large arrowhead: infiltration of inflammatory cells; small arrowhead: particle-laden macrophages; arrow: presence of NPs; and blue arrowhead: fibrosis-like changes.

and crystalline structures. Although the TiO₂NP types investigated in the study were not synthesised in a controlled manner to vary in only one property at a time, from the results of the comprehensive assessment conducted, it can be concluded that the underlying mechanisms of acute pulmonary inflammation induced by TiO₂NPs are the same regardless of their properties, which is in alignment with the previous study results published by this research group (22). Also in alignment were the results showing that while size may be the primary determinant of the toxic potential of TiO₂NPs, surface modifications influence the severity of the response with hydrophilic surface being more inflammogenic compared with the other types. Halappanavar et al. (22) compared the lung transcriptomic responses in mice exposed to rutile TiO₂NPs of 10 nm, 38 nm and 10 nm TiO₂NPs with hydrophilic surface and showed that at the transcriptional level, 10 nm particles were more responsive with highest number of DEGs. However, surface amination of 10 nm TiO₂NPs resulting in hydrophilic surface increased the severity of the response (larger fold changes in inflammation-associated genes). The extensive transcriptomic profiling and histopathological analysis conducted in the present study confirm these findings. In the present study, the number of DEGs at Day 1 post-exposure to anatase-type TiO₂NPs was remarkably lower for the ^aTiO₂³⁰⁰ with the surface area of 10 m²/g (85 genes) and was highest for the ^aTiO₂⁸ exhibiting 229–235 m²/g (225 genes). While the primary particle size may have been instrumental in the lung responses induced by the anatase type TiO₂NPs, for the rutile types [^{ra}TiO₂²⁰, ^rTiO₂²⁰ (HY) and ^rTiO₂²⁰ (HP)], mixed properties including surface modifications and crystallinity appeared to have influenced the responses. New to the present study was the finding that anatase TiO₂NPs were less responsive compared with

the rutile/anatase and rutile TiO₂NPs at the transcriptional level. Although a direct comparison of responses induced by the anatase and rutile types was not possible as they vary in their surface properties, the overall biological response of mice exposed to anatase type TiO₂NPs was less compared with the rutile ones. Previous studies have shown that crystalline structure of TiO₂NPs plays an important role in toxicity induced by these particles (16,18).

Among the rutile types, all three of them were of 20 nm in size and exhibited a surface area between 51 and 57 m²/g, which is relatively less compared with the surface area of anatase ^aTiO₂²⁰ 90 m²/g. It was observed that the number of DEGs induced by ^rTiO₂²⁰ (HY) were similar to the number of DEGs induced by ^aTiO₂²⁰; however, ^rTiO₂²⁰ (HP) induced considerably higher number of genes at all doses and post-exposure time points compared with the other rutile and anatase TiO₂NP types. These results suggest that the transcriptional responses to rutile type TiO₂NPs are influenced by their surface modifications and that the hydrophilic surface positively impacts the lung responses. Although all rutile types are similar in size and surface area, mixed rutile/anatase type exhibited significantly larger transcriptomic response at the highest dose tested. The ^{ra}TiO₂²⁰ has been previously shown to exert higher toxicity compared with the other rutile or anatase only TiO₂NPs (41–43). The higher activity of ^{ra}TiO₂²⁰ compared with that of either pure rutile type can be suggested to be due to the synergistic effects between rutile and anatase crystalline phases (44); however, this could not be confirmed since the present study did not include an unmodified rutile TiO₂ type.

The results of the gene expression analysis were in agreement in general with the BALF cellularity and inflammatory cell infiltration.

to are not identified. The results of the present study suggest that the hydrophilic surface may render TiO₂NPs with pro-fibrotic potential in the long term when exposed to sufficiently high doses.

Apart from the predominant inflammogenic gene expression changes, several genes associated with the p53 signalling pathway was found to be specifically altered following exposure to ⁸TiO₂ and ²⁰TiO₂ NPs. TEM analysis also found particles in the nucleus following exposure to ⁸TiO₂ and ²⁰TiO₂ (HP). These results suggest that some of them may have a potential to induce DNA damage. There are not many *in vivo* studies that have investigated the DNA damage potential of TiO₂NPs. It was shown that a 21-nm anatase/rutile (59) and a 33-nm ⁸TiO₂NPs (60) induce DNA damage and genetic instability in blood cells of mice exposed orally over a short period of time. Intragastric administration of 75 nm ⁸TiO₂NPs to male Sprague Dawley rats for 30 days (4) was shown to induce genotoxic effects in the bone marrow. However, positive genotoxic effects have not been observed in rodent lungs exposed to TiO₂NPs via inhalation (61,62). Although many studies have investigated the genotoxic effects of TiO₂NPs using *in vitro* models, the results are not consistent. For example, AMES assays showed no increases in the mutagenic potential of ⁸TiO₂NPs *in vitro* models. However, DNA damage analysis using comet assays showed that uncoated 20–50 nm ⁸TiO₂NPs tested at a concentration of 100 µg/mL induced DNA breaks in BEAS2B cells, bottlenose dolphin leucocytes, human gastric adenocarcinoma cells, human epidermal cells and human embryonic kidney (HEK293) cells (6,55–57). One other study showed positive DNA damage potential of 33 nm ⁸TiO₂NPs in bone marrow and liver of CBAB6F1 mice exposed via gavage (60). However, at present, the properties of TiO₂NPs or factors responsible for their DNA damaging potential are not understood.

Conclusions

In conclusion, a comprehensive assessment of lung responses was conducted following exposure to six types of TiO₂NPs exhibiting differences in size, crystalline structure and surface modifications across a range of doses and post-exposure time points. The results confirmed our previous findings that the underlying mechanisms leading to TiO₂NP-induced lung inflammation acutely after exposure are the same regardless of their properties; however, the results suggested that the long-term pathological effects may be influenced by their specific properties such as crystallinity and surface modifications. Specifically, from the six types tested, a combination of properties such as rutile structure and hydrophilic surface can be deemed as pathologically more active compared to other types. Although TiO₂NPs are generally regarded as inert, the results from the study suggest that unfavourable and chronic exposures to very high doses of certain TiO₂NP types may result in tissue injury and initiate pro-fibrotic changes in lungs over a long period of time.

Supplementary data

Supplementary Tables 1 to 7 and Supplementary Figures 1 to 8 are available at *Mutagenesis* Online.

Funding

This work was supported by Health Canada's Genomics Research and Development Initiative and Chemicals Management Plan.

Acknowledgements

We would like thank Dr Jake Nikota, Sarah Labib and Dr Ella Atlas for helpful comments on the manuscript. We are grateful to Dr Don Caldwell (Regulatory Toxicology Research Division) for histopathology analysis and to Dr Arkadiy Reunov and Peter Rippstein (University of Ottawa Heart Institute) for assistance with the electron microscopy.

Conflict of interest statement: None declared.

Reference

- Hendren, C. O., Mesnard, X., Dröge, J. and Wiesner, M. R. (2011) Estimating production data for five engineered nanomaterials as a basis for exposure assessment. *Environ. Sci. Technol.*, 45, 2562–2569.
- Sun, T. Y., Gottschalk, F., Hungerbühler, K. and Nowack, B. (2014) Comprehensive probabilistic modelling of environmental emissions of engineered nanomaterials. *Environ. Pollut.*, 185, 69–76.
- Robichaud, C. O., Uyar, A. E., Darby, M. R., Zucker, L. G. and Wiesner, M. R. (2009) Estimates of upper bounds and trends in nano-TiO₂ production as a basis for exposure assessment. *Environ. Sci. Technol.*, 43, 4227–4233.
- Chen, T., Yan, J. and Li, Y. (2014) Genotoxicity of titanium dioxide nanoparticles. *J. Food Drug Anal.*, 22, 95–104.
- Rossi, E. M., Pylkkanen, L., Koivisto, A. J., et al. (2010) Airway exposure to silica-coated TiO₂ nanoparticles induces pulmonary neutrophilia in mice. *Toxicol. Sci.*, 113, 422–433.
- Husain, M., Saber, A. T., Guo, C., et al. (2013) Pulmonary instillation of low doses of titanium dioxide nanoparticles in mice leads to particle retention and gene expression changes in the absence of inflammation. *Toxicol. Appl. Pharmacol.*, 269, 250–262.
- Fischer, H. C., Liu, L., Pang, K. S. and Chan, W.C.W. (2006) Pharmacokinetics of nanoscale quantumdots: in vivo distribution, sequestration and clearance in the rat. *Adv. Funct. Mater.*, 16, 1299–1305.
- Husain, M., Wu, D., Saber, A. T., et al. (2015) Intratracheally instilled titanium dioxide nanoparticles translocate to heart and liver and activate complement cascade in the heart of C57BL/6 mice. *Nanotoxicology.*, 9, 1013–1022.
- Liu, R., Yin, L., Pu, Y., Liang, G., Zhang, J., Su, Y., Xiao, Z. and Ye, B. (2009) Pulmonary toxicity induced by three forms of titanium dioxide nanoparticles via intra-tracheal instillation in rats. *Prog. Nat. Sci.*, 19, 573–579.
- Yang, X. N. and Cui, F. Y. (2013) Stability of nano-sized titanium dioxide in an aqueous environment: effects of pH, dissolved organic matter and divalent cations. *Water Sci. Technol.*, 68, 276–282.
- Ferin, J. and G.Oberdörster (1991) Translocation of particles from pulmonary alveoli into the interstitium. *J. Aerosol Med.*, 5, 179–187.
- Gwinn, M. R. and Vallyathan, V. (2006) Nanoparticles: health effects—pros and cons. *Environ. Health Perspect.*, 114, 1818–1825.
- Iavicoli, I., Leso, V., Fontana, L. and Bergamaschi, A. (2011) Toxicological effects of titanium dioxide nanoparticles: a review of *in vitro* mammalian studies. *Eur. Rev. Med. Pharmacol. Sci.*, 15, 481–508.
- Renwick, L., Brown, D., Clouter, A. and Donaldson, K. (2004) Increased inflammation and altered macrophage chemotactic responses caused by two ultrafine particle types. *Occup. Environ. Med.*, 61, 442–447.
- Warheit, D. B., Brock, W. J., Lee, K. P., Webb, T. R. and Reed, K. L. (2005) Comparative pulmonary toxicity inhalation and instillation studies with different TiO₂ particle formulations: impact of surface treatments on particle toxicity. *Toxicol. Sci.*, 88, 514–524.
- Warheit, D. B., Hoke, R. A., Finlay, C., Donner, E. M., Reed, K. L. and Sayes, C. M. (2007) Development of a base set of toxicity tests using ultrafine TiO₂ particles as a component of nanoparticle risk management. *Toxicol. Lett.*, 171, 99–110.
- Warheit, D. B., Borm, P. J., Hennes, C. and Lademann, J. (2007) Testing strategies to establish the safety of nanomaterials: conclusions of an ECE-TOC workshop. *Inhal. Toxicol.*, 19, 631–643.
- Warheit, D. B., Webb, T. R., Reed, K. L., Frerichs, S. and Sayes, C. M. (2007) Pulmonary toxicity study in rats with three forms of ultrafine-TiO₂

- particles: differential responses related to surface properties. *Toxicology*, 230, 90–104.
19. Sweeney, S., Berhanu, D., Ruenraroengsak, P., Thorley, A. J., Valsami-Jones, E. and Tetley, T. D. (2014) Nano-titanium dioxide bioreactivity with human alveolar type-I-like epithelial cells: Investigating crystalline phase as a critical determinant. *Nanotoxicology*, 19, 1–11.
 20. Braydich-Stolle, L. K., Schaublin, N. M., Murdock, R. C., Jiang, J., Biswas, P., Schlager, J. J. and Hussain, S. M. (2008) Crystal structure mediates mode of cell death in TiO₂ nanotoxicity. *J. Nanopart. Res.*, 11, 1361–1374.
 21. Halappanavar, S., Jackson, P., Williams, A., Jensen, K. A., Hougaard, K. S., Vogel, U., Yauk, C. L. and Wallin, H. (2011) Pulmonary response to surface-coated nanotitanium dioxide particles includes induction of acute phase response genes, inflammatory cascades, and changes in microRNAs: a toxicogenomic study. *Environ. Mol. Mutagen.*, 52, 425–439.
 22. Halappanavar, S., Saber, A. T., Decan, N., *et al.* (2015) Transcriptional profiling identifies physicochemical properties of nanomaterials that are determinants of the in vivo pulmonary response. *Environ. Mol. Mutagen.*, 56, 245–264.
 23. Manoudis, P. N., Karapanagiotis, I., Tsakalof, A., Zuburtikudis, I., Kolinkeov, C. and Panayiotou, C. (2009) Superhydrophobic films for the protection of outdoor cultural heritage assets. *Appl. Phys. A*, 97, 351–360.
 24. Zhang, L., Zhou, Z., Cheng, B., DeSimone, J. M. and Samulski, E. T. (2006) Superhydrophobic behavior of a perfluoropolyether lotus-leaf-like topography. *Langmuir*, 22, 8576–8580.
 25. Rasmussen, K., Mast, J., De Temmerman, P. J., *et al.* (2015) Titanium Dioxide, NM-100, NM-101, NM-102, NM-103, NM-104, NM-105: Characterisation and Physico-Chemical Properties. *JRC Science and Policy Reports*. Publications Office of the European Union, JRC Repository: NM-series of representative manufactured nanomaterials, Joint Research Centre, Ispra, Italy.
 26. Mie, G. (1908) Beiträge zur Optik trüber Medien, speziell kolloidaler Metallösungen. *Ann. Phys.*, 330, 377–445.
 27. Poulsen, S. S., Saber, A. T., Williams, A., *et al.* (2015) MWCNTs of different physicochemical properties cause similar inflammatory responses, but differences in transcriptional and histological markers of fibrosis in mouse lungs. *Toxicol. Appl. Pharmacol.*, 284, 16–32.
 28. Poulsen, S., Jacobsen, N. R., Labib, S., *et al.* (2013) Transcriptomic analysis reveals novel mechanistic insight into murine biological responses to multi-walled carbon nanotubes in lungs and cultured lung epithelial cells. *PLoS One*, 8, e80452.
 29. R Core Team. (2015) *R: A language and environment for statistical computing*. R Foundation for Statistical Computing, R Foundation for Statistical Computing, Vienna, Austria.
 30. Stephens, M. A. (1986). Tests based on EDF statistics. In D'Agostino, R. B. and Stephens, M. A., (eds.), *Goodness-of-Fit Techniques*. Marcel Dekker, New York, pp. 97–194.
 31. Levene, H. (1960). *Robust tests for equality of variances, in contributions to probability and statistics*. In Olkin, I. (ed.), Stanford Univ. Press, Palo Alto, CA, pp. 278–292.
 32. Conover, W. J. and Iman, R. L. (1981). Rank transformations as a bridge between parametric and nonparametric statistics. *Am. Stat.*, 35, 124–129.
 33. Kerr, M. K. (2003) Design considerations for efficient and effective microarray studies. *Biometrics*, 59, 822–828.
 34. Cui, X., Hwang, J. T., Qiu, J., Blades, N. J., and Churchill, G. A. (2005) Improved statistical tests for differential gene expression by shrinking variance components estimates 1. *Biostatistics*, 6, 59–75.
 35. Benjamini, Y. and Hochberg, Y. (1995) Controlling the false discovery rate: a practical and powerful approach to multiple testing. *J. R. Stat. Soc. B Methodol.*, 57, 289–300.
 36. Renne, R., Brix, A., Harkema, J., *et al.* (2009) Proliferative and nonproliferative lesions of the rat and mouse respiratory tract. *Toxicol. Pathol.*, 37, 5S–73S.
 37. Wang, C., Muttill, P., Lu, D., Beltran-Torres, A. A., Garcia-Contreras, L. and Hickey, A. J. (2009) Screening for potential adjuvants administered by the pulmonary route for tuberculosis vaccines. *AAPS J*, 11, 139–147.
 38. Gavett, S. H., Parkinson, C. U., Willson, G. A., Wood, C. E., Jarabek, A. M., Roberts, K. C., Kodavanti, U. P. and Dodd, D. E. (2016) Persistent effects of Libby amphibole and amosite asbestos following subchronic inhalation in rats. *Part. Fibre Toxicol.*, 13, 1–20.
 39. Edelson, J. D., Shannon, J. M. and Mason, R. J. (1988) Alkaline phosphatase: a marker of alveolar type II cell differentiation. *Am Rev Respir Dis*, 138, 1268–1275.
 40. Inoue, K.-I., Koike, E., Yanagisawa, R. and Takano, H. (2010) Extensive analysis of elastase-induced pulmonary emphysema in rats: ALP in the lung, a new biomarker for disease progression? *J. Clin. Biochem. Nutr.*, 46, 168–176.
 41. Gerloff, K., Fenoglio, I., Carella, E., Kolling, J., Albrecht, C., Boots, A. W., Forster, I. and Schins, R. P. (2012) Distinctive toxicity of TiO₂ rutile/anatase mixed phase nanoparticles on Caco-2 cells. *Chem. Res. Toxicol.*, 25, 646–655.
 42. Armand, L., Dagouassat, M., Belade, E., *et al.* (2013) Titanium dioxide nanoparticles induce matrix metalloproteinase 1 in human pulmonary fibroblasts partly via an interleukin-1beta-dependent mechanism. *Am. J. Respir. Cell Mol. Biol.*, 48, 354–363.
 43. Abbott Chalew, T. E. and Schwab, K. J. (2013) Toxicity of commercially available engineered nanoparticles to Caco-2 and SW480 human intestinal epithelial cells. *Cell Biol. Toxicol.*, 29, 101–116.
 44. Su, R., Bechstein, R., Sø, L., Vang, R. T., Sillassen, M., Esbjörnsson, Palmqvist, A. and Besenbacher, F. (2011) How the Anatase-to-rutile ratio influences the photoreactivity of TiO₂. *J. Phys. Chem. C*, 115, 24287–24292.
 45. Teubl, B. J., Schimpel, C., Leitinger, G., Bauer, B., Frohlich, E., Zimmer, A. and Roblegg, E. (2015) Interactions between nano-TiO₂ and the oral cavity: impact of nanomaterial surface hydrophilicity/hydrophobicity. *J. Hazard. Mater.*, 286, 298–305.
 46. Teubl, B. J., Leitinger, G., Schneider, M., Lehr, C. M., Frohlich, E., Zimmer, A. and Roblegg, E. (2015) The buccal mucosa as a route for TiO₂ nanoparticle uptake 2. *Nanotoxicology*, 9, 253–261.
 47. Wang, J. and Fan, Y. (2014) Lung injury induced by TiO₂ nanoparticles depends on their structural features: size, shape, crystal phases, and surface coating. *Int. J. Mol. Sci.*, 15, 22258–22278.
 48. Panariti, A., Miserochi, G. and Rivolta, I. (2012) The effect of nanoparticle uptake on cellular behavior: disrupting or enabling functions? *Nanotechnol. Sci. Appl.*, 5, 87–100.
 49. Curtis, E. M., Bahrami, A. H., Weikl, T. R. and Hall, C. K. (2015) Modeling nanoparticle wrapping or translocation in bilayer membranes. *Nanoscale*, 7, 14505–14514.
 50. Snyder-Talkington, B. N., Dymacek, J., Porter, D. W., *et al.* (2013) System-based identification of toxicity pathways associated with multi-walled carbon nanotube-induced pathological responses. *Toxicol. Appl. Pharmacol.*, 272, 476–489.
 51. Bermudez, E., Mangum, J. B., Asgharian, B., Wong, B. A., Reverdy, E. E., Janszen, D. B., Hext, P. M., Warheit, D. B. and Everitt, J. I. (2002) Long-term pulmonary responses of three laboratory rodent species to subchronic inhalation of pigmentary titanium dioxide particles 4. *Toxicol. Sci.*, 70, 86–97.
 52. Bermudez, E., Mangum, J. B., Wong, B. A., Asgharian, B., Hext, P. M., Warheit, D. B. and Everitt, J. I. (2004) Pulmonary responses of mice, rats, and hamsters to subchronic inhalation of ultrafine titanium dioxide particles 5. *Toxicol. Sci.*, 77, 347–357.
 53. Moran, C. A., Mullick, F. G. and Ishak, K. G. (1991) Identification of titanium in human tissues: probable role in pathologic processes. *Human Pathol.*, 22, 450–454.
 54. Keller, C. A., Frost, A., Cagle, P. T. and Abraham, J. L. (1995) Pulmonary alveolar proteinosis in a painter with elevated pulmonary concentrations of titanium. *Chest*, 108, 277–280.
 55. Botelho, M. C., Costa, C., Silva, S., Costa, S., Dhawan, A., Oliveira, P. A. and Teixeira, J. P. (2014) Effects of titanium dioxide nanoparticles in human gastric epithelial cells in vitro 185. *Biomed. Pharmacother.*, 68, 59–64.
 56. Ghosh, M., Chakraborty, A. and Mukherjee, A. (2013) Cytotoxic, genotoxic and the hemolytic effect of titanium dioxide (TiO₂) nanoparticles

- on human erythrocyte and lymphocyte cells in vitro. *J. Appl. Toxicol.*, 33, 1097–1110.
57. Valdiglesias, V., Costa, C., Sharma, V., Kilic, G., Pasaro, E., Teixeira, J. P., Dhawan, A. and Laffon, B. (2013) Comparative study on effects of two different types of titanium dioxide nanoparticles on human neuronal cells. *Food Chem. Toxicol.*, 57, 352–361.
58. Yamadori, I., Ohsumi, S. and Taguchi, K. (1986) Titanium dioxide deposition and adenocarcinoma of the lung. *Acta Pathol. Jpn.*, 36, 783–790.
59. Trouiller, B., Reliene, R., Westbrook, A., Solaimani, P. and Schiestl, R. H. (2009) Titanium dioxide nanoparticles induce DNA damage and genetic instability in vivo in mice. *Cancer Res.*, 69, 8784–8789.
60. Sycheva, L. P., Zhurkov, V. S., Iurchenko, V. V., Dauge-Dauge, N. O., Kovalenko, M. A., Krivtsova, E. K. and Durnev, A. D. (2011) Investigation of genotoxic and cytotoxic effects of micro- and nanosized titanium dioxide in six organs of mice in vivo. *Mutat. Res.*, 726, 8–14.
61. Landsiedel, R., Ma-Hock, L., van Ravenzwaay, B., Schulz, M., Wiench, K., Champ, S., Schulte, S., Wohlleben, W. and Oesch, F. (2010) Gene toxicity studies on titanium dioxide and zinc oxide nanomaterials used for UV-protection in cosmetic formulations. *Nanotoxicology*, 4, 364–381.
62. Lindberg, H. K., Falck, G. C., Catalan, J., et al. (2012) Genotoxicity of inhaled nanosized TiO₂ in mice. *Mutat. Res.*, 745, 58–64.